

# Data-driven Quantum Dynamical Embedding Method for Long-term Prediction on Near-term Quantum Computers

Tai-Ping Sun,<sup>1,2</sup> Zhao-Yun Chen,<sup>3,\*</sup> Cheng Xue,<sup>3</sup> Huan-Yu Liu,<sup>1,2</sup> Xi-Ning Zhuang,<sup>1,2,4</sup>  
Yun-Jie Wang,<sup>5</sup> Shi-Xin Ma,<sup>1,6</sup> Hai-Feng Zhang,<sup>1,2</sup> Yu-Chun Wu,<sup>1,2,3,†</sup> and Guo-Ping Guo<sup>1,2,3</sup>

<sup>1</sup>Key Laboratory of Quantum Information, Chinese Academy of Sciences, School of Physics, University of Science and Technology of China, Hefei, Anhui, 230026, P. R. China

<sup>2</sup>CAS Center For Excellence in Quantum Information and Quantum Physics, University of Science and Technology of China, Hefei, Anhui, 230026, P. R. China

<sup>3</sup>Institute of Artificial Intelligence, Hefei Comprehensive National Science Center, Hefei, Anhui, 230088, P. R. China

<sup>4</sup>Origin Quantum Computing, Hefei, Anhui, 230026, P. R. China

<sup>5</sup>Institute of Advanced Technology, University of Science and Technology of China, Hefei, Anhui, 230031, P. R. China

<sup>6</sup>National Innovation Institute of Defense Technology, AMS, Beijing, 100071, P. R. China

The increasing focus on long-term time series prediction across various fields has been significantly strengthened by advancements in quantum computation. In this paper, we introduce a data-driven method designed for long-term time series prediction with quantum dynamical embedding (QDE). This approach enables a trainable embedding of the data space into an extended state space, allowing for the recursive retrieval of time series information. Based on its independence of time series length, this method achieves depth-efficient quantum circuits that are crucial for near-term quantum computers. Numerical simulations demonstrate the model's improved performance in prediction accuracy and resource efficiency over existing methods, as well as its effective denoising capabilities. We implement this model on the Origin "Wukong" superconducting quantum processor with a learnable error-cancellation layer (LECL) for error mitigation, further validating the practical applicability of our approach on near-term quantum devices. Furthermore, the theoretical analysis of the QDE's dynamical properties and its universality enhances its potential for time series prediction. This study establishes a significant step towards the processing of long-term time series on near-term quantum computers, integrating data-driven learning with discrete dynamical embedding for enhanced forecasting capabilities.

## I. INTRODUCTION

Recent years have witnessed a surge in the application of time series prediction across a range of fields, including finance, physics, and engineering, underscoring its significance [1–3]. Among the various types of predictions, long-term prediction is especially pivotal as it entails forecasting future values of a series that extend beyond the duration of the available historical data. This means that the prediction horizon is longer than the time span of the training dataset, presenting a unique challenge in identifying and extrapolating underlying patterns and trends that may continue to evolve over time [4, 5]. The importance of long-term prediction is evident in strategic planning for climate change, economic forecasting, and technological forecasting, where decisions made today are based on projections that reach far into the future [6, 7]. Classical algorithms for time series prediction predominantly rely on long short-term memory (LSTM) networks [8, 9], echo state networks (ESNs) [10, 11], and reservoir computing (RC) [12]. These data-driven methods have shown potential in capturing dynamical features. Recently, it has been demonstrated that classical data can be mapped into a quantum feature space using certain embeddings [13–16], which is further utilized to approximate a variety of functions. These universal approximation properties [17–20] facilitate the construction of inference functions for modeling temporal data patterns, suggesting the potential of quantum

systems to effectively model the complex dynamics inherent in long-term time series.

Current quantum algorithms for time series processing, such as quantum reservoir computing (QRC) [21–32], quantum recurrent neural networks (QRNNs) [33–35], and quantum dynamic mode decomposition (QDMD) [36], have demonstrated significant potential in understanding temporal dependencies in sequential data. However, QRC and QRNNs exhibit a linear increase in circuit depth as the length of the time sequence grows, posing challenges for noisy intermediate-scale quantum (NISQ) devices. The increasing circuit depth threatens the maintenance of quantum coherence over time, which is crucial for the accuracy of long-term predictions. Although the QRC model has shown significant performance of time series prediction, its requirement for deep circuits to maintain temporal dependencies makes it impractical for NISQ devices due to exacerbated decoherence and noise, which undermine the performance of quantum algorithms in realistic settings. Efficiently utilizing these devices for complex tasks like long-term time series prediction without deep circuits is essential for advancing practical quantum computing applications. Therefore, there is a pressing need for methods that can predict long-term time series with shallow quantum circuits, addressing the limitations posed by current quantum hardware. Solutions have been explored through both theoretical and physical implementations on various platforms [37–43], yet it remains an open question.

In this study, we present a data-driven approach for time series prediction using quantum dynamical embedding (QDE). Specifically, we recurrently retrieve time series data from strong measurements of the QDE at the current time step.

\* chenzhaoyun@ia.i.ustc.edu.cn

† wuyuchun@ustc.edu.cn

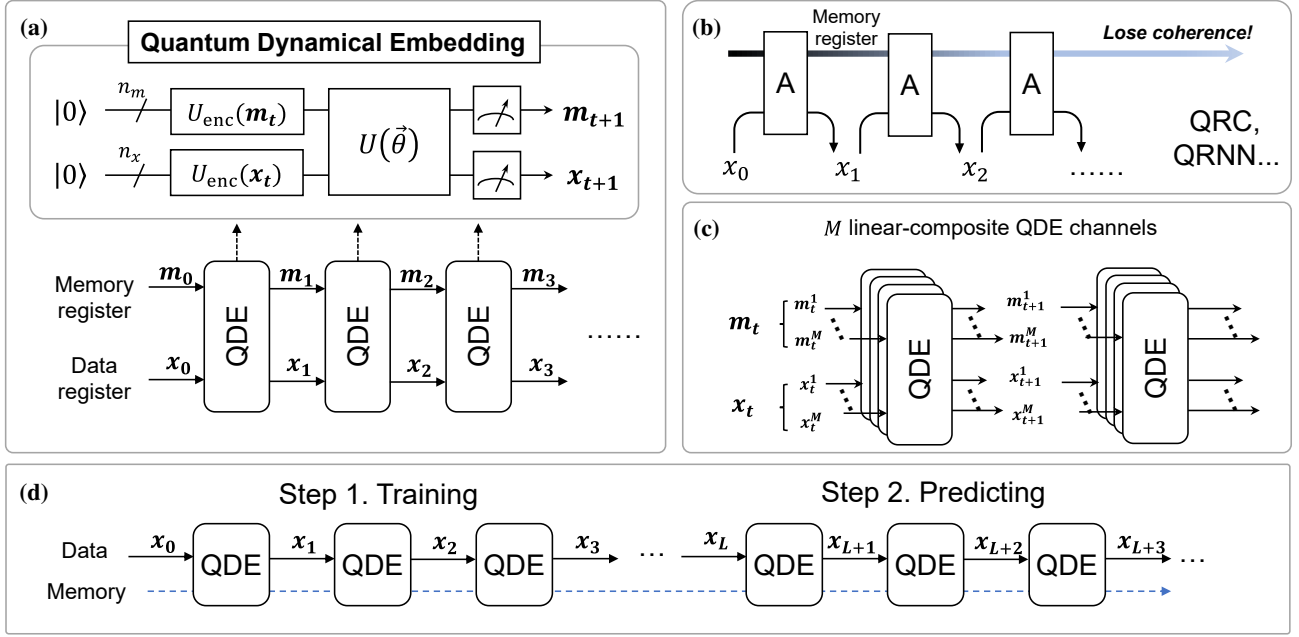


FIG. 1. **Circuits for QDE and Learning Protocols.** (a) Illustration of a generic QDE architecture. The qubits for encoding the classical state are divided into two sets: the memory register (top, with  $n_m$  qubits) for inputting memory  $m_t$ , and the data register (bottom, with  $n_x$  qubits) for inputting data  $x_t$  at time  $t$ . The circuit then undergoes evolution through a unitary operator  $U(\theta)$ , comprising parametrized quantum gates and fixed Hamiltonian evolution across  $D$  layers. Finally, selected observable ensembles are measured to extract classical information. With this architecture and the initial point  $(m_0, x_0)$ , the state pairs  $(m_1, x_1), (m_2, x_2), (m_3, x_3), \dots$  are obtained in an autoregressive way. (b) The protocol of QRC and QRNNs. The data is injected into the quantum system and measured to retrieve classical information. The memory register maintains the quantum state form and will lose coherence in the long run. (c) An enhanced QDE architecture with  $M$  linear-composite channels. In this design, the QDE is available to explore the dynamics with higher degrees of freedom. The final signal  $x_t$  is retrieved through the superposition of sub-signals  $x_t^1, \dots, x_t^M$  from different channels. (d) Training and predicting protocols. In the training stage, initial data  $x_0$  is fed into the QDE block, and the output data  $\hat{x}_i$  is used to compute the cost function, with  $i = 1, \dots, L$  and time updated over  $L$  steps. After the training, the system undergoes an additional  $T$  steps of evolution to predict future values. Note that while the memory evolves simultaneously with the data in both stages, it does not contribute to the cost function calculation.

Our approach allows for the dynamic embedding of original data into an extended state space and facilitates the data-driven learning of embedding parameters. This method offers a solution for long-term time series prediction with circuit depth independent of the time series length and mitigates issues related to decoherence and error accumulation over time.

Embedding serves as an effective strategy for converting from non-Markovian to Markovian dynamics by expanding the hidden space, allowing for a more flexible representation of temporal data. This enlargement is pivotal for revealing the intricate dynamics and temporal patterns inherent in the series. Furthermore, the flexibility to choose the size of the extended hidden space and the trainability of the embedding parameters are particularly advantageous for long-term time series prediction, ensuring a data-driven approach that adapts to the complexity of the data at hand.

We demonstrate the effectiveness of our method through numerical experiments with cosine-wave and composite signals. Additionally, we evaluate its denoising capabilities on the same prediction tasks when exposed to random noise, further showcasing the QDE's versatility. Notably, a comparative analysis with existing methodologies reveals that our approach offers significant advantages in terms of average pre-

diction accuracy and computational efficiency on the same tasks. This improvement highlights the robustness of our approach in capturing temporal dependencies more effectively than existing quantum models.

To validate the noise resistance of our method, we perform long-term predictions using a noisy simulator with a learnable error-cancellation layer (LECL) following the QDE. Additionally, we extend our implementation to the Origin "Wukong" superconducting quantum computer, integrating an LECL to generate time series. This demonstrates the potential of leveraging current quantum computing capabilities for real-world time series prediction challenges.

Theoretically, we explore the dynamics of a specific 2-qubit case, providing insights into the connection between the QDE and the inherent characteristics of time series. We present several theorems that underscore the universality of the QDE in this context. Finally, we adopt an autoregressive model in our approach because it allows us to utilize past observations to predict future values, which is a natural fit for time series data. The autoregressive framework aligns well with the principles of QDE, enabling efficient and accurate long-term predictions while maintaining the practical constraints of NISQ devices. Overall, this study advances our understanding of practical

time series processing on near-term quantum devices, paving the way for more effective applications in quantum computing.

## II. METHOD

### A. The quantum dynamical embedding model

The common target among different time series prediction tasks can be viewed as learning the complex system's dynamics from a huge size of historical data. Markovian dynamics can be characterized by the iteration,  $\mathbf{x}_{t+1} = f(\mathbf{x}_t)$ , where  $f(\cdot)$  represents the update function, and  $\mathbf{x}_t, \mathbf{x}_{t+1}$  represent the system state at time steps  $t$  and  $t + 1$ , respectively. In more complex non-Markovian scenarios, a memory architecture is necessary to maintain the autonomous nature of the system:  $(\mathbf{x}_{t+1}, \mathbf{m}_{t+1}) = \mathcal{F}(\mathbf{x}_t, \mathbf{m}_t)$ , where  $\mathcal{F}(\cdot)$  denotes the extended update function,  $\mathbf{m}_t$  and  $\mathbf{m}_{t+1}$  denote the hidden states at time steps  $t$  and  $t + 1$ , respectively. Such an embedding, from the low-dimensional yet non-Markovian space of original data into a high-dimensional Markovian phase space, has shown great power in RC, ESNs, and recurrent neural networks [8, 9, 11, 12, 44–46].

However, this embedding procedure turns out to be too expansive when training a highly non-Markovian process with a quickly growing phase space. Fortunately, quantum systems, due to their exponentially large Hilbert space, can be leveraged as a work memory to encode and evolve the phase space [34, 37, 38, 40]. Nevertheless, there are still two essential weaknesses faced by all of the works mentioned above: Firstly, a long-term coherence needs to be preserved which seems formidable in the NISQ era. Secondly, the circuit depth grows at least linearly in those approaches, inducing a strong restriction on any further long-term training or predicting procedures.

To address this issue, we propose a classical-quantum hybrid protocol to learn and predict long-term time series, wherein only fixed-depth circuits are employed, and long-term training and predicting are enabled, as shown in Fig. 1. More specifically, for each step, given the hidden memory  $\mathbf{m}_t$  of size  $n_m$  and the observable data  $\mathbf{x}_t$  of size  $n_x$ , a shallow parameterized quantum circuit  $(n_m, n_x)$ -QDE is applied to the input pair  $(\mathbf{m}_t, \mathbf{x}_t)$

$$|\psi_t\rangle = U(\boldsymbol{\theta})|\mathbf{m}_t\rangle_m|\mathbf{x}_t\rangle_x, \quad (1)$$

where

$$|\mathbf{m}_t\rangle_m|\mathbf{x}_t\rangle_x = (U_{\text{enc}}(\mathbf{m}_t)|0\rangle_m) \otimes (U_{\text{enc}}(\mathbf{x}_t)|0\rangle_x)$$

is the encoded input state.  $U(\boldsymbol{\theta})$  is a trainable parameterized quantum circuit. The memory and data of the next step are extracted from observing of their corresponding subspaces, namely

$$\mathbf{m}_{t+1} = \text{Tr}(\mathcal{H}_m|\psi_t\rangle\langle\psi_t|), \quad (2)$$

and

$$\mathbf{x}_{t+1} = \text{Tr}(\mathcal{H}_x|\psi_t\rangle\langle\psi_t|), \quad (3)$$

where  $\mathcal{H}_m$  and  $\mathcal{H}_x$  are the observable vector with length  $n_m$  and  $n_x$ , respectively.

This process gives a mapping from  $(\mathbf{m}_t, \mathbf{x}_t)$  to  $(\mathbf{m}_{t+1}, \mathbf{x}_{t+1})$ , which is denoted as  $\text{QDE}(\mathbf{m}_t, \mathbf{x}_t; \boldsymbol{\theta}) \mapsto (\mathbf{m}_{t+1}, \mathbf{x}_{t+1})$ . Given any parameterized quantum circuit  $U(\boldsymbol{\theta})$  and the initial state  $(\mathbf{m}_0, \mathbf{x}_0)$ , one could keep performing this mapping to obtain  $\mathbf{x}_1, \mathbf{x}_2, \dots, \mathbf{x}_\infty$ , as illustrated in Fig. 1(a).

The QDE distinguishes itself from previous studies of QRC and QRNNs in the manner of memory information storage. Unlike these models, where the quantum system serves as a memory reservoir for historical data, our approach overcomes the issue of coherence loss—a challenge in long-term data embedding and retrieval—through the QDE model, as illustrated in Fig. 1(b).

Enhancements to the QDE model are achieved by integrating  $M$  linear-composite channels, as shown in Fig. 1(c). Each channel in the QDE utilizes the architecture in Fig. 1(a), albeit with distinct parameters. These channels are designed to contain identical qubit numbers for both data and memory registers. The final output,  $\mathbf{x}_t$ , is a synthesis of sub-signals  $\mathbf{x}_t^1, \dots, \mathbf{x}_t^M$  from these varied channels, enabling the QDE to explore dynamics with increased degrees of freedom.

### B. Training and predicting

As we can see from the QDE model, with a fixed circuit  $U(\boldsymbol{\theta})$  and the initial point, we can determine the evolution of this system. Given the trainability of the parameterized quantum circuit, we can employ a data-driven method for predicting the time series. That is, we utilize historical data points to develop a model that accurately represents the underlying patterns in the data. Once this model is established, we extrapolate it over time to forecast future trends and values. The training of the model can be formulated as

**Definition 1** (Training a data-driven model). *Given a trainable predictive model  $\mathcal{F}(\mathbf{x}, \mathbf{m}; \boldsymbol{\theta})$ , where  $\mathbf{x}$  denotes the data,  $\mathbf{m}$  the hidden memory,  $\boldsymbol{\theta}$  the trainable parameters, and a standard historical dataset  $\mathbf{x}_{0:L}$ , where  $\mathbf{x}_{0:L}$  represents the series of data points from time 0 to  $L$ . Use this model to sequentially generate a predicted data  $\hat{\mathbf{x}}_{0:L}$  from the initial point  $\mathbf{x}_0$ . The objective is to optimize the parameter  $\boldsymbol{\theta}$ , formulated as*

$$\text{argmin}_{\boldsymbol{\theta}} \mathcal{L}(\hat{\mathbf{x}}_{0:L}, \mathbf{x}_{0:L}; \boldsymbol{\theta})$$

where  $\mathcal{L}$  quantifies the difference between the predicted and historical series.

In the subsequent applications, the QDE is optimized using mean square error (MSE) as the loss function, defined as:

$$\mathcal{L}_{\text{mse}} = \frac{1}{L} \sum_{t=1}^L \|\mathbf{x}_t - \hat{\mathbf{x}}_t\|_2^2, \quad (4)$$

where the  $\hat{\mathbf{x}}_t$  and  $\mathbf{x}_t$  denote the time series values at time step  $t$  for  $\hat{\mathbf{x}}_{0:L}$  and  $\mathbf{x}_{0:L}$ , respectively. The term  $\|\cdot\|_2$  represents the  $L^2$  norm.

Building on the findings of previous research, the embedding of time series and the evolving of quantum systems require a circuit depth of  $\mathcal{O}(L)$ . Comparatively, our approach marks a notable advancement by achieving this with a significantly reduced circuit depth of  $\mathcal{O}(\Gamma)$ , where  $\Gamma$  represents the base depth of a single QDE circuit block.

Moreover, we employ gradient descent for circuit parameter optimization, with the number of circuit executions scaling as  $\mathcal{O}(nL)$ , where  $n = n_m + n_x$  denotes the total qubit number in the QDE. The linear dependency on the time series length  $L$  facilitates the use of gradient-based optimization methods. For an in-depth discussion of this procedure, see Sec. II C.

After training, the iterative mapping is applied over  $T$  additional steps for prediction, generating the series  $\hat{\mathbf{x}}_{L+1:L+T}$  to approximate target values. In the subsequent tests, we compare the prediction results with the ideal results to show the performance of the QDE. The predicting error is also defined as MSE.

### C. Gradient evaluation

The optimal parameters for the QDE are obtained by minimizing the loss function, as expressed in Eq. (4). During the training stage, the initial state vector  $(\mathbf{m}_0, \mathbf{x}_0)$  at time

$t = 0$  is composed of the given initial data  $\mathbf{x}_0$  and its complementary component  $\mathbf{m}_0$ , which is initialized randomly. This state vector is then fed into the QDE block, yielding a time sequence  $\{(\mathbf{m}_1, \hat{\mathbf{x}}_1), \dots, (\mathbf{m}_L, \hat{\mathbf{x}}_L)\}$ , with the explicit part represented as  $\{\hat{\mathbf{x}}_1, \dots, \hat{\mathbf{x}}_L\}$ . To simplify the illustration, we focus on a 2-qubit QDE, where both the given data and the memory are scalars. The loss function is then reformulated as  $\mathcal{L}_{mse} = \frac{1}{L} \sum_{t=1}^L (\hat{x}_t - x_t)^2$ . The derivative of  $\mathcal{L}_{mse}$  with respect to  $\theta_i$  is given by:

$$\frac{\partial \mathcal{L}_{mse}}{\partial \theta_i} = \frac{2}{L} \sum_{t=1}^L (\hat{x}_t - x_t) \frac{\partial \hat{x}_t}{\partial \theta_i}. \quad (5)$$

Referring to the definition of  $\hat{x}_{t+1}$  in Eq. (3), this expression can be equivalently written as:

$$\begin{aligned} \frac{\partial \hat{x}_{t+1}}{\partial \theta_i} &= \frac{\partial}{\partial \theta_i} \text{Tr}(\mathcal{H}_x |\psi_t\rangle \langle \psi_t|) \\ &= \frac{\partial}{\partial \theta_i} \text{Tr} \left[ \mathcal{H}_x U(\boldsymbol{\theta}) U_{enc}(\hat{X}_t) \rho_0 U_{enc}^\dagger(\hat{X}_t) U^\dagger(\boldsymbol{\theta}) \right], \end{aligned} \quad (6)$$

where  $\hat{X}_t = (m_t, \hat{x}_t)$  and  $\rho_0 = (|0\rangle\langle 0|)^{\otimes n}$  for simplicity. It is important to note that both  $U(\boldsymbol{\theta})$  and  $U_{enc}(\hat{X}_t)$  depend on  $\theta_i$ . Hence, the derivative of Eq. (6) is:

$$\begin{aligned} \frac{\partial \hat{x}_{t+1}}{\partial \theta_i} &= \text{Tr} \left[ \mathcal{H}_x \frac{\partial U(\boldsymbol{\theta})}{\partial \theta_i} U_{enc}(\hat{X}_t) \rho_0 U_{enc}^\dagger(\hat{X}_t) U^\dagger(\boldsymbol{\theta}) \right] + \text{Tr} \left[ \mathcal{H}_x U(\boldsymbol{\theta}) U_{enc}(\hat{X}_t) \rho_0 U_{enc}^\dagger(\hat{X}_t) \frac{\partial U^\dagger(\boldsymbol{\theta})}{\partial \theta_i} \right] \\ &+ \text{Tr} \left[ \mathcal{H}_x U(\boldsymbol{\theta}) \frac{\partial U_{enc}(\hat{X}_t)}{\partial \theta_i} \rho_0 U_{enc}^\dagger(\hat{X}_t) U^\dagger(\boldsymbol{\theta}) \right] + \text{Tr} \left[ \mathcal{H}_x U(\boldsymbol{\theta}) U_{enc}(\hat{X}_t) \rho_0 \frac{\partial U_{enc}^\dagger(\hat{X}_t)}{\partial \theta_i} U^\dagger(\boldsymbol{\theta}) \right]. \end{aligned} \quad (7)$$

The first two terms on the right-hand side of Eq. (7) can be computed using the parameter shift rule [47], as the rotation gates are generated with Pauli operators, e.g.,  $R_Y(\theta_i) = e^{-i\theta_i/2\sigma_y}$ . Assuming that the encoding gates are also Pauli-

generated unitaries and that the function  $u(x) = \arccos(x)$  is designed to convert state to rotation angle, the remaining terms on the right-hand side of Eq. (7) can be computed as follows:

$$\begin{aligned} \frac{\partial U_{enc}(\hat{X}_t)}{\partial \theta_i} &= \frac{\partial U_{enc}(m_t)}{\partial \theta_i} \otimes U_{enc}(\hat{x}_t) + U_{enc}(m_t) \otimes \frac{\partial U_{enc}(\hat{x}_t)}{\partial \theta_i} \\ &= \frac{\partial U(u)}{\partial u} \frac{\partial u(m_t)}{\partial m_t} \frac{\partial m_t}{\partial \theta_i} \otimes U_{enc}(\hat{x}_t) + U_{enc}(m_t) \otimes \frac{\partial U(u)}{\partial u} \frac{\partial u(\hat{x}_t)}{\partial \hat{x}_t} \frac{\partial \hat{x}_t}{\partial \theta_i} \\ &= \left( -\frac{1}{\sqrt{1-m_t^2}} \cdot \frac{\partial m_t}{\partial \theta_i} \right) \frac{\partial U(u)}{\partial u} \otimes U_{enc}(\hat{x}_t) + \left( -\frac{1}{\sqrt{1-\hat{x}_t^2}} \cdot \frac{\partial \hat{x}_t}{\partial \theta_i} \right) U_{enc}(m_t) \otimes \frac{\partial U(u)}{\partial u}. \end{aligned} \quad (8)$$

Together with its conjugate term  $\partial U_{enc}^\dagger(\hat{X}_t)/\partial \theta_i$ , each term in the last equation of Eq. (8) can be efficiently calculated using the parameter shift rule. This is because the coefficients can be evaluated with the current values of  $m_t$ ,  $\hat{x}_t$ , and previous values of  $\partial m_t/\partial \theta_i$ ,  $\partial \hat{x}_t/\partial \theta_i$ . Thus, while the gradient of

$\hat{x}_{t+1}$  with respect to variable  $\theta_i$  depends on all previous time steps, the gradient for a single time step can be computed in 6 evaluations based on the parameter shift rule, provided that the partial derivatives  $\partial m_t/\partial \theta_i$ ,  $\partial \hat{x}_t/\partial \theta_i$  are computed in order  $t = 1, 2, \dots, L$ . Since  $m_{t+1}$  is obtained with the same



quantum circuit as  $\hat{x}_t$  but with a different measurement  $\mathcal{H}_m$ , computing  $\partial m_t / \partial \theta_i$  will not increase the number of evaluations. The total complexity for computing  $\partial L / \partial \theta_i$  is  $\mathcal{O}(nL)$ .

Our proposed model QDE avoids the barren plateau issue in quantum neural networks (QNNs) by utilizing multiple independent channels of QDE block with shallow circuit depths and weak entanglement. The shallow circuits limit the entanglement within each channel, preventing the volume-law scaling of entanglement that leads to barren plateaus [48]. Furthermore, the independence of channels reduces overall entanglement, decreasing the likelihood of encountering regions with vanishing gradients in the optimization landscape [49]. This design ensures a more navigable optimization landscape, enabling efficient and reliable training of the quantum neural network. Therefore, QDE's structure effectively mitigates the barren plateaus in QNNs, providing a robust framework for quantum time series predictions [50].

#### D. Experimental settings

The quantum circuit of the QDE comprises three primary components: encoding, parametrized evolution, and quantum measurement, as detailed in Sec. II A. To simplify the QDE circuit, we implement the encoding layer  $U_{enc}(\cdot)$  with rotation  $R_Y^i(\arccos(\cdot))$  for the  $i^{\text{th}}$  qubit. Here,  $R_Y(\cdot)$  is defined as  $R_Y(\theta) = e^{-i\frac{\theta}{2}\sigma_y}$ , with the input normalized to the range  $[-1, 1]^{\otimes n}$ . Furthermore, the observables  $\mathcal{H}_m, \mathcal{H}_x$  are designed as  $\sigma_z$  for the respective qubit. This design choice is driven by the understanding that the input can be efficiently reconstructed using the  $\sigma_z$  expectation, eliminating the need for additional evolution. As the number of qubits, circuit depth, and linear-composite channels increase, the QDE exhibits more complex dynamics. The methodology for scaling these elements is depicted in Fig. 1(c) and properties are further discussed in Sec. III D. Throughout the time sequence iterations, all quantum circuit parameters remain constant.

The QDE's circuit architecture is tailored to match the complexity of the specific task at hand. In our study, we propose two distinct quantum circuit architectures: the transverse Ising evolution ansatz (TIEA) and the hardware-efficient ansatz (HEA).

**TIEA:** This architecture is designed to enhance the expressiveness of each ansatz layer. The unitary operator  $U(\theta)$  includes sequential single-qubit rotations followed by a Hamiltonian evolution applied across the entire circuit. The single-qubit rotations are defined by the equation:

$$U_1(\theta_1, \theta_2, \theta_3) = R_X(\theta_1)R_Z(\theta_2)R_X(\theta_3), \quad (9)$$

with  $\theta_1, \theta_2$ , and  $\theta_3$  as real parameters from the set  $\theta$ , and  $R_X$  and  $R_Z$  as single-qubit rotations around the x and z axes, expressed as  $R_X(\theta) = e^{-i\frac{\theta}{2}\sigma_x}$  and  $R_Z(\theta) = e^{-i\frac{\theta}{2}\sigma_z}$ , respectively. These rotations are followed by a Hamiltonian evolution, denoted as  $e^{-iH\tau}$ , where  $\tau$  signifies the evolution time and  $H$  the Hamiltonian, specified as in previous

works [25, 34, 51]:

$$H = \sum_{i=1}^n (h + D_i)\sigma_{x,i} + \sum_{i=2}^n \sum_{j=1}^{i-1} J_{ij}\sigma_{z,i}\sigma_{z,j}, \quad (10)$$

where  $h$  represents the transverse field strength and  $J_{ij}$  denotes the coupling strength of site  $i$  and  $j$ . The coefficients  $D_i, J_{ij}$  are randomly chosen from a uniform distribution within  $[-W, W]$  and  $[-J_s, J_s]$ , respectively. And all remain fixed during training.

**HEA [52]:** This architecture utilizes a CZ entanglement layer combined with single-qubit rotations  $U_1$  as described in TIEA. In the specific case of a 2-qubit QDE, the architecture simplifies to a CZ gate followed by single-layer parametrized  $R_Y$  rotations, which are then utilized in the prediction of composite signals.

### III. RESULTS

#### A. Applications

This part establishes both numerical and experimental evidence on some applications to characterize the adaptability of the QDE introduced above. Firstly, we employ the QDE to predict a cosine-wave signal with a single channel. In the context of composite signal functions, our approach effectively captures the characteristics inherent in superpositions of different cosine-wave signals with the architecture depicted in Fig. 1(c). To further demonstrate the QDE's versatility, we assess its denoising capability on signals exposed to uniform noise. For benchmarking purposes, we compare it with the performance using QRC. Additionally, we focus on long-term time series and noisy simulations, training and forecasting them at a ratio of 1 : 10 under the influence of depolarizing or amplitude-damping noise. Notably, an experimental test on a superconducting quantum computer indicates significant promise for real-world time series processing.

We employ the HEA architecture in this application and tailor the number of linear-composite channels to align with the task's complexity.

*a. Cosine-wave signal* Firstly, we apply the QDE on the cosine-wave signal,

$$x(t) = A \cos(\omega t + \phi),$$

where  $\omega = 0.04\pi$ ,  $A = 0.5$  and  $\phi = 0$  for simplicity. In this application, the QDE configuration is simplified to a single channel comprising two qubits. We define the temporal domain as  $0 \leq t \leq 200, t \in \mathbb{N}$ . In this and the following demonstrations, we train the QDE with the first 100 points generated from the equation (light red dots) and test the extrapolation prediction result for the next 100 points (blue triangles), as depicted in Fig. 2(a). The prediction error, defined by the MSE, is  $1.10 \times 10^{-5}$ , which demonstrates the capability of QDE to accurately represent the periodic nature of the cosine-wave. Detailed theoretical foundations of these observations are further elaborated in Sec. III D.

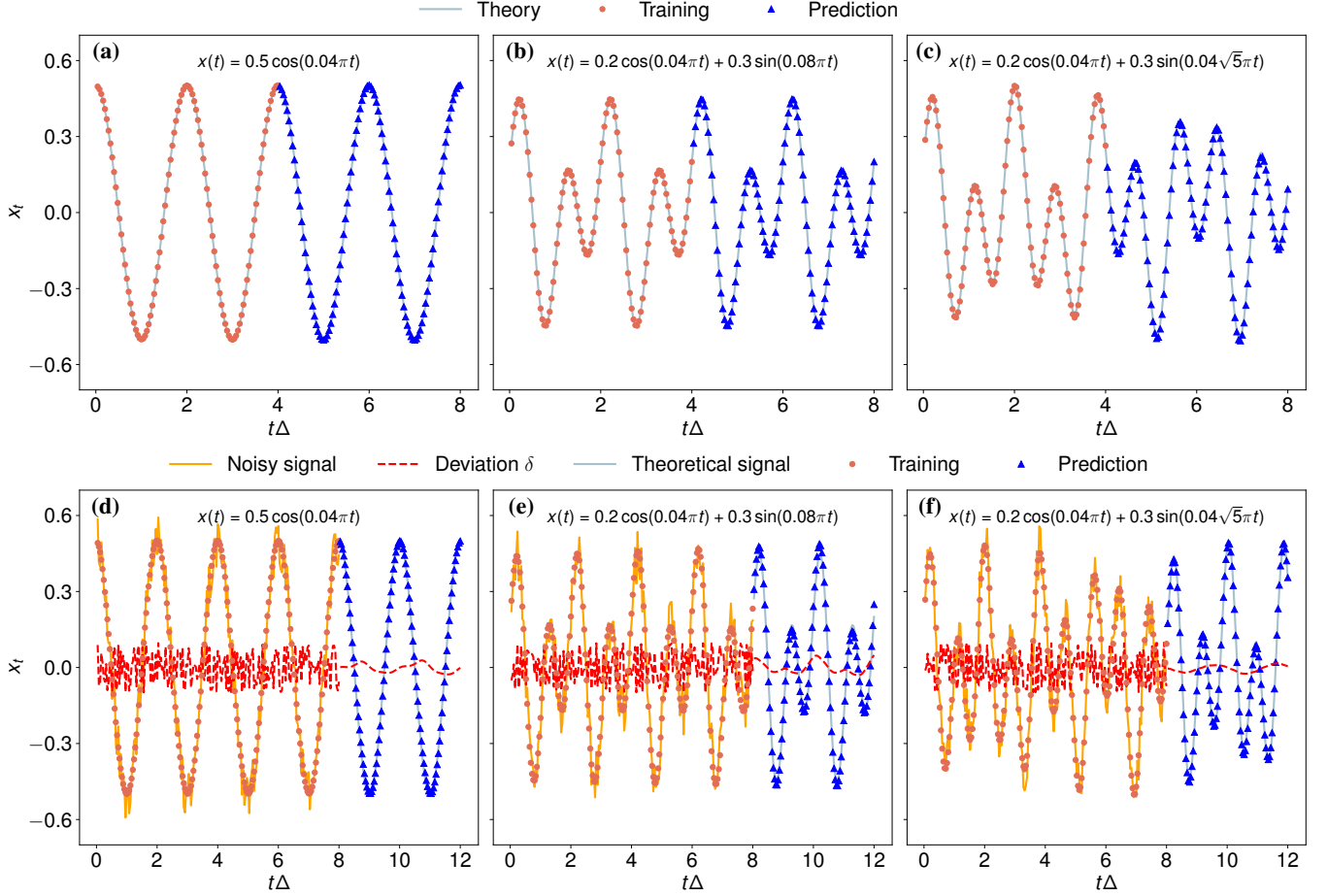


FIG. 2. **Demonstrations of QDE for Time Series Prediction:** (a) 2-qubit QDE application on cosine-wave prediction with  $x(t) = 0.5 \cos(\omega t)$ , where  $\omega = \pi/25$  and the value of time axis is rescaled by  $\Delta = 0.04$ . The training and predicting lengths are set to  $L = T = 100$  in this and the following tests. (b) Composite periodic signal predicting,  $x(t) = 0.2 \cos(\omega t) + 0.3 \sin(2\omega t)$ , where  $\omega = \pi/25$ . (c) Aperiodic time series predicting,  $x(t) = 0.2 \cos(\omega t) + 0.3 \sin(\sqrt{5}\omega t)$ , with the same architecture and settings as (b). (d), (e), and (f) correspond to the noisy versions of the scenarios described in (a), (b), and (c), respectively, trained with noise uniformly distributed within  $[-0.1, 0.1]$ . For these versions, the number of training points is increased to enhance the capture of signal characteristics buried in noise. The prediction part of each subplot is juxtaposed with theoretical clean signals for comparison. The red dashed line represents the deviation  $\delta = \hat{x}(t) - x_{\text{ref}}(t)$ , where  $\hat{x}(t)$  is the output of the QDE model and  $x_{\text{ref}}(t)$  is the reference, the noisy signal in training stage and theoretical signal in predicting stage.

*b. Composite signals* We consider applying the QDE on the composite cosine-waves

$$x(t) = \sum_i A_i \cos(\omega_i t + \phi_i),$$

where each term represents an independent wave component. In Fig. 2(b) and (c), we demonstrate two cases, a periodic and an aperiodic one with only two linear-composite channels, which can be viewed as two simplest non-trivial examples to benchmark the model. In the first case, we set  $\omega_1 = 0.04\pi$  and  $\omega_2 = 2\omega_1$ ; the second case,  $\omega_1 = 0.04\pi$  and  $\omega_2 = \sqrt{5}\omega_1$ . The corresponding prediction errors are  $5.21 \times 10^{-6}$  and  $8.10 \times 10^{-5}$ , respectively. In both cases, each channel of the QDE follows the ansatz configuration used in cosine-wave prediction. The decent performance on prediction error proved that the QDE correctly learned the systems' dynamics.

*c. Denoising of signals* To evaluate the denoising capability of the QDE, we expose the aforementioned three signals to uniform noise randomly distributed within the range of  $[-0.1, 0.1]$ . Each noisy signal undergoes processing via the QDE to evaluate its efficacy in recovering the original, clean signal. The number of training points in these versions is increased to enhance the capture of signal characteristic mode buried in random noise. For the cosine-wave, the QDE markedly reduces noise interference, achieving a denoising MSE of  $3.07 \times 10^{-3}$ , as illustrated in Fig. 2(d). Likewise, the periodic and aperiodic composite signals demonstrate the QDE's robustness in noise reduction, recording MSEs of  $3.97 \times 10^{-3}$  and  $3.21 \times 10^{-3}$ , respectively, as shown in Fig. 2(e) and (f). The prediction part of each subplot is juxtaposed with theoretical clean signals for comparison. We define the deviation as  $\delta = \hat{x}(t) - x_{\text{ref}}(t)$ , which represents

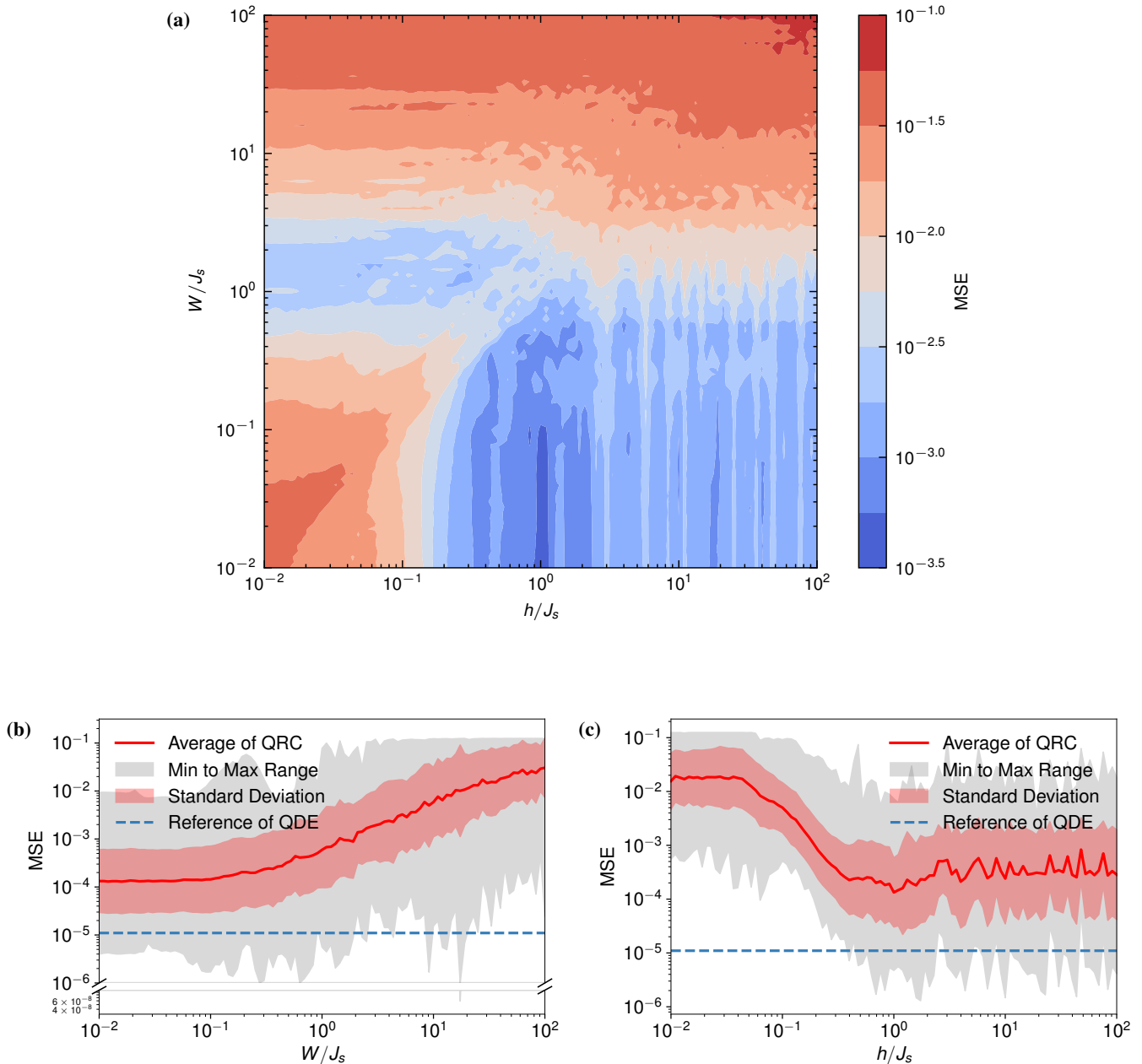


FIG. 3. **Comparison of QDE with QRC on Cosine-Wave Signal Prediction.** (a) Error map for different values of the Hamiltonian hyperparameters of QRC, with the transverse field  $h$  and the disorder bound  $W$  varying logarithmically in the range  $[10^{-2}, 10^2]$ . Results are averaged over 100 realizations. (b) and (c) With  $h/J_s$  ( $W/J_s$ ) fixed at the minimum error from map (a), the other parameter  $W/J_s$  ( $h/J_s$ ) is varied. The average results are shown with the minimum to maximum error range (grey shadows) and standard deviation (red shadows). The QDE model's performance is consistently below the average error and standard deviation of the QRC model.

the difference between the output of the QDE ( $\hat{x}(t)$ ) and the reference signal value ( $\hat{x}(t)$ ). Although  $\delta$  is random and large during the training stage, as indicated by the red dashed line, the QDE effectively extracts the noise-free mode from the signal, showcasing its notable performance in denoising. These results not only underscore the QDE's effectiveness in signal fidelity restoration but also highlight its utility in practical noise reduction scenarios.

*d. Comparison with QRC* In this application, we compare the performance of the QDE and QRC models on the aforementioned tasks. For the QRC model, we utilize a 3-qubit system with 5 evolution slices ( $V = 5$ ), keeping the training and prediction lengths consistent with those of the QDE model. The results of this comparison for the first task, cosine-wave signal prediction, are shown in Fig. 3(a)-(c). The error map for different values of the Hamiltonian

hyper-parameters of QRC is plotted with the transverse field  $h$  and the disorder bound  $W$  varying logarithmically in the range  $[10^{-2}, 10^2]$ . Results are averaged over 100 realizations. Fig. 3(b) and Fig. 3(c) demonstrate that when  $h/J_s$  ( $W/J_s$ ) is fixed at the minimum error from the map in Fig. 3(a) and the other parameter  $W/J_s$  ( $h/J_s$ ) varies in the range  $[10^{-2}, 10^2]$ , the MSE of the QDE model, indicated by the dashed light blue line, consistently remains below the average error (red curve) and standard deviation (red shadows) of the QRC model. Despite some instances of lower prediction error across 100 realizations, the 2-qubit QDE model exhibits more stable performance in terms of precision, circuit depth, and training resource allocation compared to the QRC model. Further results on the other two tasks, along with detailed insights into the QRC theory and its configurations, can be found in the supplementary information.

### B. Performing long-term prediction by recovering from noisy results

In this part, we show how the QDE can be applied to noisy quantum computers. As analyzed above, the long-term coherence of qubits need to be kept for the QRC and QRNN models. As a result, the long-term prediction task turns to be formidable due to the strong sensitivity to noise. Here, we propose a trainable method to recover the system from noisy results. Moreover, we show that our method can allow the QDE to spontaneously unbiased the difference among different quantum computers.

First, we analyze the effect of noise for a QDE running on a noisy quantum computer with typical error sources, including the depolarizing, the amplitude-damping, and the readout error. We denote the noiseless and actual results for qubit  $i$  as  $\langle \sigma_z^i \rangle^*$  and  $\langle \sigma_z^i \rangle$ , respectively.

For the depolarizing noise, let  $\sigma$  be the initial quantum state,  $\rho^{(k)}$  the state after  $k$  applications of the depolarizing and unitary channels, and  $\rho$  the state absent noise channels. We can express  $\rho^{(k)}$  as:

$$\rho^{(k)} \equiv \left[ \left( \prod_{j=1}^k \mathcal{U}_j \circ \mathcal{E}_{p_j}^{\mathcal{D}} \right) \right] \circ \sigma, \quad (11)$$

where  $p_j$  represents the probability of the depolarizing channel  $\mathcal{E}_{p_j}^{\mathcal{D}}$  and  $\mathcal{U}_j(\cdot) = U_j \cdot U_j^\dagger$  represents the unitary channel.

Drawing from Lem. 1 in [53], this is reformulated as:

$$\begin{aligned} \rho^{(k)} &= \left( \prod_{j=1}^k (1 - p_j) \right) U_k \cdots U_1 \sigma U_1^\dagger \cdots U_k^\dagger \\ &+ \left( 1 - \prod_{j=1}^k (1 - p_j) \right) \frac{I}{2^n} \\ &= \prod_{j=1}^k (1 - p_j) \rho + \left( 1 - \prod_{j=1}^k (1 - p_j) \right) \frac{I}{2^n}. \end{aligned} \quad (12)$$

Subsequently, the noisy result  $\langle \sigma_z^i \rangle$  is represented as:

$$\begin{aligned} \langle \sigma_z^i \rangle &= \text{Tr}[\rho^{(k)} \sigma_z^i] \\ &= \left( \prod_{j=1}^k (1 - p_j) \right) \langle \sigma_z^i \rangle^*. \end{aligned} \quad (13)$$

For the amplitude damping noise, characterized by the amplitude damping channel  $\mathcal{E}_\gamma^{\text{AD}}$ , it affects the quantum state  $\rho$  like:

$$\begin{aligned} \langle \sigma_z^i \rangle &= \text{Tr}[\mathcal{E}_\gamma^{\text{AD}}(\rho) \sigma_z^i] \\ &= (1 - \gamma) \langle \sigma_z^i \rangle^* + \gamma, \end{aligned} \quad (14)$$

where  $\gamma$  is the strength of the amplitude damping channel.

For the readout error, this can be understood as a probabilistic transformation of ideal measurement results. Specifically, the readout error can be characterized as bit-flip events, which is quantified using a response matrix  $M$ . The observed outcome probabilities, denoted as  $\mathbf{p}_{\text{obs}}$ , are obtained from the transformation of the error-free probabilities  $\mathbf{p}_{\text{ideal}}$  as follows:

$$\mathbf{p}_{\text{obs}} = M \mathbf{p}_{\text{ideal}}. \quad (15)$$

Given that the observable  $\sigma_z^i$  can be decomposed into projectors of computational bases, it is feasible to express the result with readout error as the combination of elements from  $\mathbf{p}_{\text{obs}}$ , further as the linear transformation on the ideal result. This is similar to what is observed in depolarizing and amplitude damping scenarios.

To enhance the recovery of results from noisy quantum computers, we introduce a linear layer called LECL, consisting of a linear transformation with parameters  $A : \mathbb{R}^{n \times n}$ ,  $\mathbf{b} : \mathbb{R}^n$ . This layer performs the mapping  $(\mathbf{x}, \mathbf{m})^T \mapsto A(\mathbf{x}, \mathbf{m})^T + \mathbf{b}$  on the obtained measurements within  $n^2 + n$  parameters. The computational complexity of training and inference with this linear layer remains within  $\mathcal{O}(n^2)$ , facilitated by the implementation of the back-propagation algorithm [44]. Notably, since this procedure operates within classical computational frameworks, it does not increase the number of executions required for the quantum circuits. We emphasize that the quantum process should still be the resource of the ability of this model, instead of this linear layer. A model comprising only the linear layer, without the QDE, lacks non-linearity and is therefore unsuitable for most problems.

We evaluated long-term prediction capabilities of the QDE under aforementioned noise channels using a cosine-wave signal and two composite signals. Maintaining a training-to-predicting ratio of 1 : 10 and replicating previous settings, including the LECL, these simulations highlight the robustness of the QDE complemented by a linear layer. This robustness demonstrates the QDE's potential for long-term time series prediction in practical scenarios.

The numerical results also demonstrate the models' stability under different noise strengths, showcasing the main benefit of this error-recovery QDE method: the system is trained not only to capture dynamical features but also to adapt to the system's noise characteristics. Due to the efficiency of the



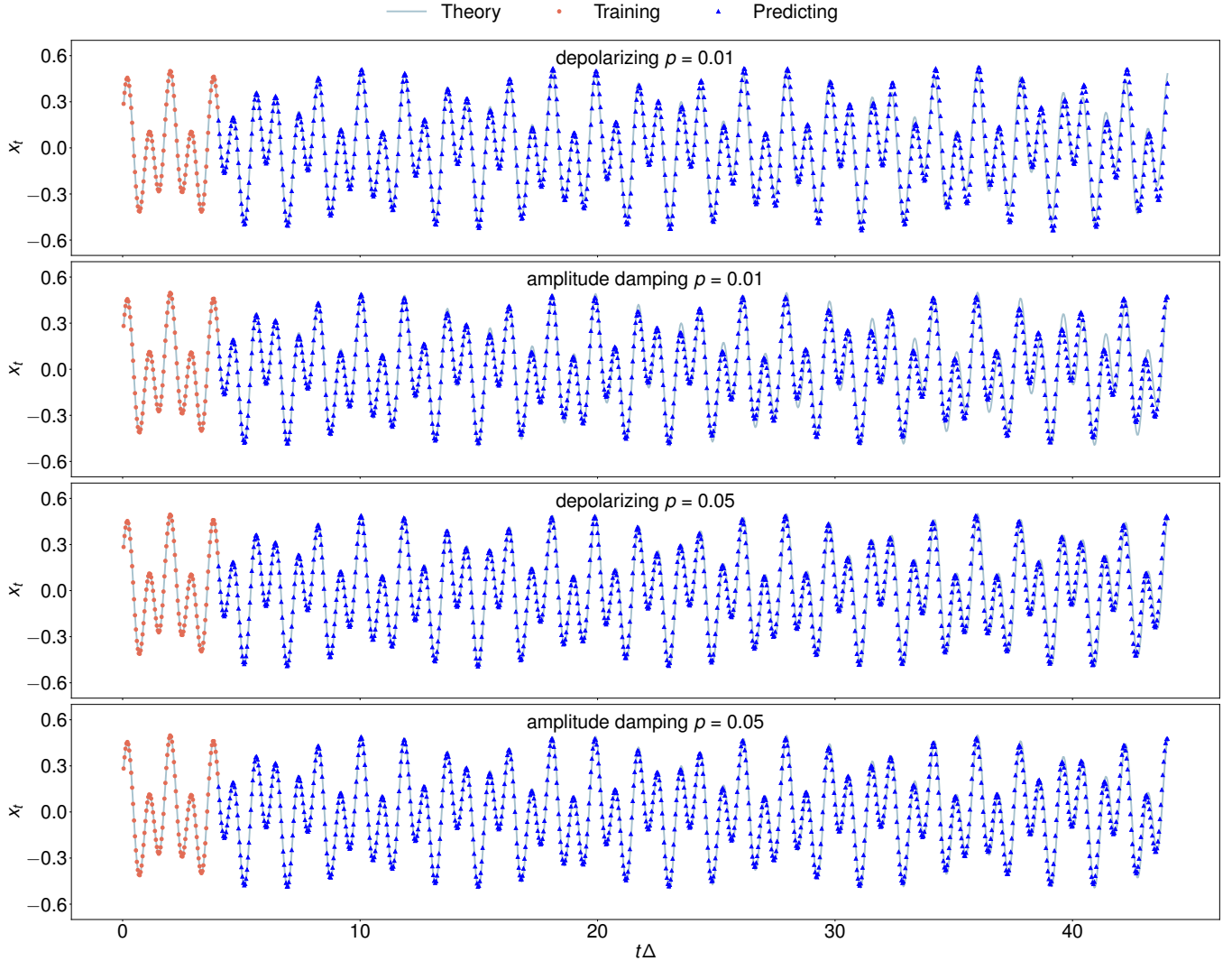


FIG. 4. **Long-term Prediction on Composite Aperiodic Signal with Quantum Noise.** The training and predicting protocols replicate those in Fig. 2, with the distinction of a training-to-predicting ratio of 1 : 10.

training algorithm, we achieve enhanced adaptability without incurring additional costs.

### C. Experimental demonstration on a superconducting quantum processor

As previously discussed, the realization of time series predictions is challenged by different typical errors. Our approach addresses these compounded errors by focusing on the mitigation of gate and readout errors with LECL method. This focus is crucial for maintaining accuracy in our model, as the fixed circuit depth does not increase with the time series length, making gate and readout error mitigation paramount regardless of decoherence.

Previous studies have developed error mitigation techniques to refine expectation values on quantum computers [54–58]. In this experimental demonstration on the Origin

“Wukong” platform, we utilize a 2-qubit system for cosine-wave prediction. We leverage a learning-based error mitigation approach, integrated with learnable error-cancellation layer as previously described, considering only gate and readout errors. Different from the direct error model determination and probabilistic correction in [54, 55], we aim to average errors within the encoding space, establishing a transformation between noiseless results and those obtained from near-term quantum computers. This transformation is vital in error compensation during time series forecasting.

To further elaborate, we consider executing quantum circuits with grid inputs  $m^i, x^i$  in the state space  $m, x \in [-1, 1]$ . The discrepancy between the ideal outputs,  $(m^*, x^*) = \text{QDE}(m, x)$ , and actual outputs from the quantum processor without LECL,  $(\hat{m}, \hat{x})$ , is quantified as  $\epsilon_m = \hat{m} - m^*$  and  $\epsilon_x = \hat{x} - x^*$ . Subsequently, an LECL characterized by parameters  $A$  and a bias vector  $\mathbf{b}$  is applied to the experimental results within this state space. These parameters are opti-

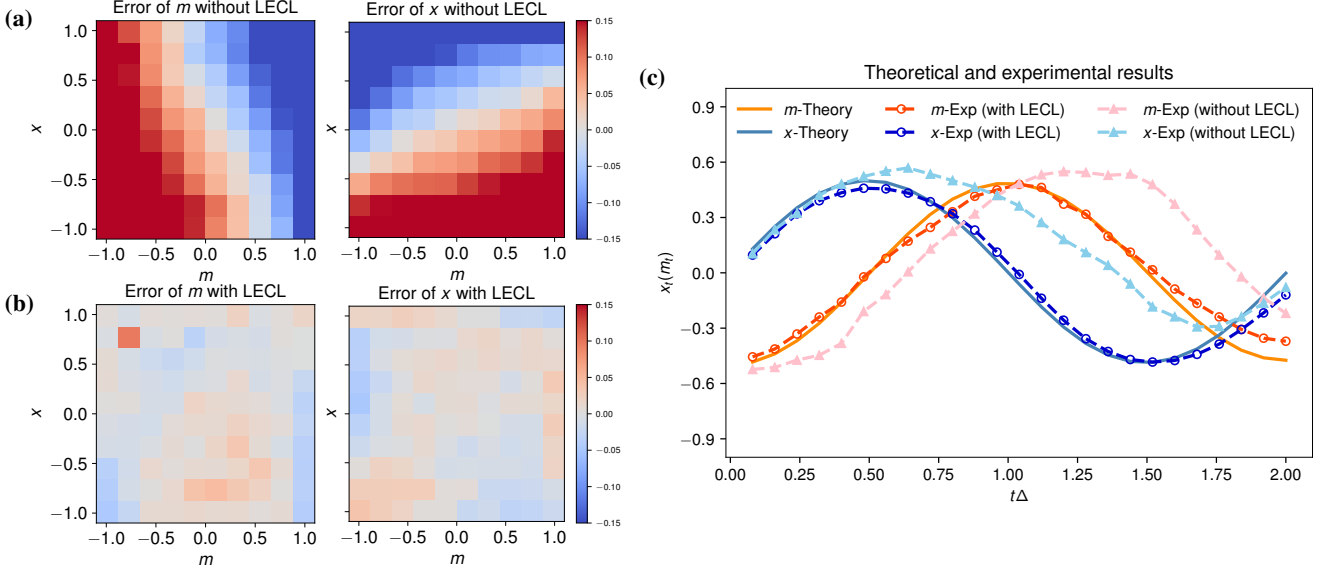


FIG. 5. **Error Distribution in Encoding Space and the Cosine-wave Signal Generation.** (a) Error distribution within the encoding space  $(m, x)$ , each grid point indicating the deviation between the ideal output  $(m^*, x^*)$  and the quantum computer’s output  $(\hat{m}, \hat{x})$  without LECL, denoted as  $\epsilon_m = \hat{m} - m^*$  and  $\epsilon_x = \hat{x} - x^*$ . (b) Adjusted error distribution following the application of LECL, illustrating the changes in error magnitude. (c) Generation of a single period of a cosine-wave time series, showing the data register dynamics and the memory register responses; solid lines correspond to the results from ideal simulations with optimized parameters, while dashed lines represent the outcomes from the quantum computer after the LECL is applied.

mized with Broyden-Fletcher-Goldfarb-Shanno (BFGS) algorithm [59–62], implemented in SCIPY [63], and fixed for the time series generation. Utilizing these optimized parameters, we construct a 25-step time sequence that aligns with a single period of cosine-wave.

The experiments are performed on the “Wukong” quantum processor of the Origin platform and reveal the error distribution with and without LECL, depicted in Fig. 5(a) and (b). Comparative analysis of error distributions before and after applying the optimization procedure reveals that errors are reduced to below the threshold of  $10^{-2}$ . Consequently, the time series can be reconstructed using the optimized linear transformation. As demonstrated in Fig. 5(c), this error mitigation technique effectively prevents divergence in the time series data, validating the feasibility of the QDE on NISQ platforms and marking a significant advance in quantum-based time series analysis.

#### D. Dynamics analysis

The classical dynamics exhibit a variety of characteristics, whereas the properties of quantum dynamical embedding remain less explicit. An in-depth analysis of classical dynamical properties, such as periodicity and fixed points, facilitates a foundational understanding of the QDE and enhances the learnability of data-driven methods. Nevertheless, dynamical analysis necessitates an explicit formulation of the QDE, a task that becomes increasingly complex with higher qubit number or greater circuit depth.

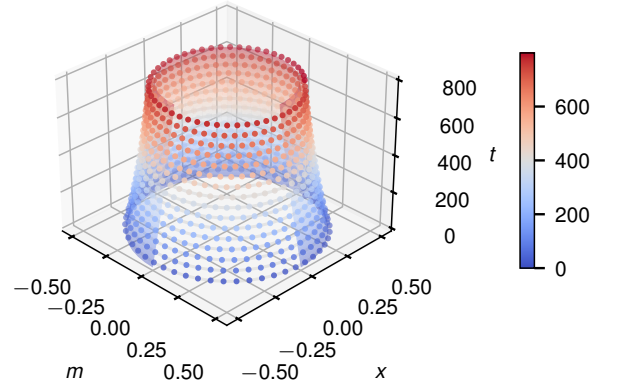


FIG. 6. **Comparison of QDE Trajectory and Its Linear Approximation.** The trajectory generated by the QDE of Eq. (16) extends along the timeline, while the surface is plotted based on the dynamics of Eq. (17) with parameters set to  $(a^*, b^*, \gamma^*)$ .

Utilizing a simplified (1, 1)-QDE architecture with HEA construction which is used in Sec. III A for cosine-wave prediction, we derive the theoretical mapping equations as follows:

$$\begin{cases} m_{t+1} = m_t \cos \theta_1 - x_t \sqrt{1 - m_t^2} \sin \theta_1, \\ x_{t+1} = x_t \cos \theta_2 - m_t \sqrt{1 - x_t^2} \sin \theta_2. \end{cases} \quad (16)$$

In subsequent analysis, we treat the given data  $x_{t+1}$  and

its estimator  $\hat{x}_{t+1}$  as equivalent within a generative model framework, not distinguishing between them. Although quantum computation operates linearly with unitary quantum operators, it is possible to derive a nonlinear discrete map of the state vector. This nonlinearity, evident as a square root in Eq. (16), arises from encoding and measurement protocols. Nonetheless, analyzing nonlinear dynamical systems typically involves identifying fixed points and linearizing the system in a small neighborhood, a technique that loses efficacy when initial values are distant from these points, limiting its applicability across the entire phase plane. While identifying the fixed point at  $(0, 0)$  of  $(1, 1)$ -QDE is straightforward, linear properties in its neighborhood can not extend to the global phase space.

Considering a specific scenario where  $\theta_2 = -\theta_1 = \theta > 0$  and  $x, m \in [-0.5, 0.5]$ , the square root terms in Eq. (16) range from 0.866 to 1.0. To linearize the equations, we replace the square root with a constant  $\gamma \in (0.866, 1.0)$ , transforming Eq. (16) into a matrix form  $(m_{t+1}, x_{t+1})^T = R(m_t, x_t)^T$ , where  $R$  is the Jacobi matrix:

$$R = b \begin{bmatrix} \cos a & \gamma \sin a \\ -\gamma \sin a & \cos a \end{bmatrix}, \quad (17)$$

with  $a$  being an angle correction and  $b$  an amplitude correction relative to 1. The eigenvalues of  $R$  are  $\lambda_{\pm} = b(\cos a \pm i\gamma \sin a)$ . Optimizing  $(a, b, \gamma)$  for an initial point  $(m_0, x_0) = (0, 0.5)$  and a fixed  $\theta = 0.04\pi$  (corresponding to the angular frequency of a cosine-wave, as discussed in Sec. III A), we find that  $|\lambda_{\pm}| < 1$  for optimal values  $(a^*, b^*, \gamma^*) = (0.12754, 0.9996, 0.9973)$ . This implies that the fixed point  $(0, 0)$  is a stable focus, and the system's dynamics will converge to it over extended evolution.

A more concise expression of the discrete map can be achieved by rescaling the matrix as  $R = \beta \tilde{R}$ , where  $\beta = b\sqrt{\cos^2 a + \gamma^2 \sin^2 a} < 1$  and  $\tilde{R}$  is an orthogonal matrix:

$$\tilde{R} = \begin{bmatrix} \cos \alpha & \sin \alpha \\ -\sin \alpha & \cos \alpha \end{bmatrix}, \quad (18)$$

with  $\alpha = \arctan(\gamma \arctan(a))$ . For a given initial point  $(m_0, x_0)^T$ , the state after  $t$  iterations is  $(m_t, x_t)^T = \beta^t \tilde{R}^t (m_0, x_0)^T$ , leading to a norm  $|(m_t, x_t)^T| = |\beta^t \tilde{R}^t (m_0, x_0)^T| = \beta^t |(m_0, x_0)^T|$ . This reveals that the trajectory on the phase plane follows a logarithmic spiral, as illustrated in Fig. 6. The trajectory generated by the QDE is bounded by the surface formed by the linear dynamics of Eq. (17), validating the reasonability of our linear approximation in the presence of weak nonlinearity.

Adjusting the observables of quantum circuits allows for the simulation of similar dynamics. Introducing a scalar  $\mu$  to the right-hand side of Eq. (16), the Jacobi matrix becomes  $\mu R = \mu\beta \tilde{R}$ , yielding eigenvalues  $\lambda_{\pm} = \mu\beta(\cos \alpha \pm i\gamma \sin \alpha)$ . By tuning  $\mu$ , we can ensure the eigenvalue norms are equal to or greater than 1, indicating that the fixed point is either a center or an unstable focus, respectively.

The preceding analysis elucidates the theoretical basis for the  $(1, 1)$ -QDE model's ability to simulate the cosine-wave.

This capability primarily stems from the QDE's weak nonlinearity, which, when combined with non-Markovian memory, enables a precise approximation of the cosine-wave signal.

## E. Universality

In this section, we explore the universal applicability of the QDE in addressing a wide range of dynamical problems, with a specific focus on signal approximation.

### 1. Universality in the regime of signal approximation

We initiate our discussion by considering QDE's ability to model a cosine-wave signal. The equations governing the QDE are shown in Eq. (16). Here,  $\theta_1$  and  $\theta_2$  are parameters that can be adjusted to model the signals  $x(t) = A \cos(\omega t) = A \cos(\pi \Delta t)$  and  $m(t) = A \sin(\omega t) = A \sin(\pi \Delta t)$ , subject to amplitude  $A < 1/2$ ,  $t \in \mathbb{N}$  and time step length  $\Delta < 1/20$ . Let  $\theta_1 = -\theta < 0$  and  $\theta_2 = \theta > 0$ , then we have the following lemmas.

**Lemma 1.** *From a precise step  $m(t) = \hat{m}(t)$  and  $x(t) = \hat{x}(t)$ , the error produced in the next step is less than  $|\pi\Delta|/4$ .*

**Lemma 2.** *For an erroneous step  $\hat{m}(t) = m(t) + \delta_m$  and  $\hat{x}(t) = x(t) + \delta_x$ , suppose  $|\pi\Delta| < 1/4$ , the error produce in the next step is less than  $\delta + \frac{1}{4}|\pi\Delta|$  where  $\delta = \max(|\delta_m|, |\delta_x|)$ .*

Proofs of Lem. 1 and Lem. 2 can be found in the supplementary information (See Supplementary Detailed Proofs).

These two lemmas establish the error propagation from both an error-free initial point and an erroneous initial point to the next time step. Building on these foundational lemmas, we present the following theorems:

**Theorem 1** (Single mode cosine-wave approximation). *By properly selecting  $\theta_1$  and  $\theta_2$ , QDE can approximate  $A \cos(\pi\Delta t + \phi)$ , where  $|A| < 1/2$ ,  $|\pi\Delta| < 1/4$  with a bounded error increasing linearly over time steps.*

**Theorem 2** (Composite cosine-wave approximation). *Given a composite signal formed by the superposition of multiple cosine-waves,  $\sum_i^K A_i \cos(\omega_i t + \phi_i)$ , where each term has a distinct amplitude  $A_i$ , frequency  $\omega_i$  and phase  $\phi_i$ . A  $K$ -channel QDE can approximate this composite signal with a bounded error by properly selecting parameters  $\theta_1^1, \theta_2^1, \dots, \theta_1^K, \theta_2^K$ , with each superscript indexing the corresponding channel.*

In Thm. 1, we proved the QDE's capability to approximate a single mode cosine-wave signal with a bounded error. This establishes the potential for QDE to approximate composite cosine-wave signals, as further explored in Thm. 2. Proofs are provided in the supplementary information (supplementary Detailed Proofs).

Lastly, we present a theorem that shows the universality of the QDE based on preceding discussions:

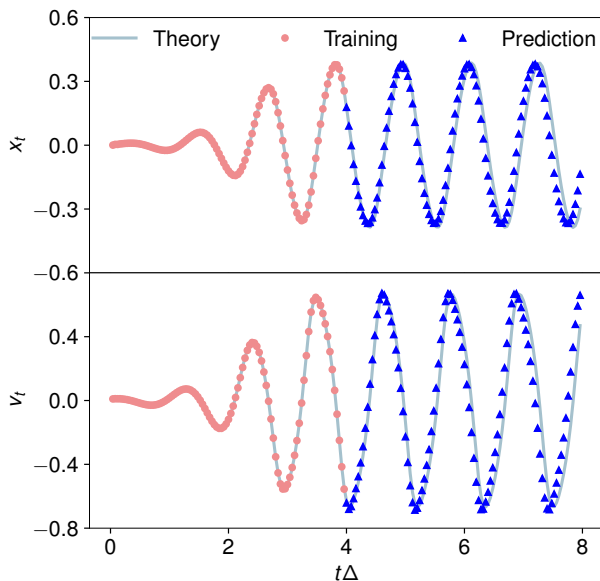


FIG. 7. **Simulation of Rayleigh Dynamics Using a (1,2)-QDE.** This diagram illustrates the dynamics of the Rayleigh system, focusing on displacement  $x_t$  and the velocity  $v_t$ , which constitute the data register in the QDE. An additional qubit is allocated for the memory register.

**Theorem 3** (Approximating any continuous function). *If  $g(t)$  is continuous on an interval  $[a, b]$ , then there exists a  $K$ -channel QDE approximating  $g(t)$  with a bounded error for any  $t$  in  $[a, b]$ .*

The proof is located in the supplementary information.

Through these lemmas and theorems, we underscore the universality of QDE in accurately modeling a wide range of signals, thereby reinforcing its potential in time series prediction.

## 2. Ability for learning from non-linear dynamics

We also demonstrate the learnability on the Rayleigh equation, a cornerstone in the study of nonlinear dynamics. We use the van der Pol form of the Rayleigh equation [64]:

$$\ddot{x} - \varepsilon \dot{x}(1 - \delta x^2) + \omega^2 x = 0, \quad (19)$$

where  $x$  is the position,  $\varepsilon$  and  $\delta$  represent the nonlinearity and damping strength, and  $\omega$  is the angular frequency.

Introducing the velocity  $v$ , Eq. (19) can be recast as a system:

$$\begin{cases} \dot{x} = v, \\ \dot{v} = \varepsilon v(1 - \delta x^2) - \omega^2 x. \end{cases} \quad (20)$$

To learn the dynamics of Rayleigh equation, the QDE model employs two qubits as the data register and one qubit as the memory register. This demonstration utilizes the ansatz TIEA as described in Sec. II D. For the Rayleigh system, we set the parameters at  $\varepsilon = \pi$ ,  $\delta = 3$ , and  $\omega = \pi$ , initializing the system with  $x_0 = (0, 0.01)$ . Fig. 7 presents the results, depicting two panels that represent  $x(t)$  and  $v(t)$  over time. The QDE model not only replicates the dynamics of the Rayleigh system but also exhibits consistent performance, closely following the ideal trajectory throughout the simulation.

## IV. DISCUSSION

In this research, we have developed a data-driven method that unites quantum machine learning with the analysis of dynamical systems in discrete time. The QDE provides a perspective of dynamical maps for understanding quantum systems and the characteristics of time series.

Distinct from existing quantum-based methods for time series prediction, our method offers a practical solution for near-term quantum computers. It addresses the significant challenge of quantum decoherence, a common obstacle in deep quantum circuits, by employing the QDE within a fixed circuit depth. This design ensures that the circuit complexity does not increase with the length of the time series, making QDE particularly suited for current NISQ devices. Through numerical simulations and practical experiments, our method has proven effective in both long-term predicting capability and noise-resilient in practical scenarios.

Looking forward, the QDE lays a robust foundation for future explorations into the complex behaviors of systems with shallow quantum circuits. This paper paves the way to merge quantum time series algorithms with the study of dynamic systems, stepping into a new avenue for understanding the physical characteristics inherent to time series prediction.

## V. ACKNOWLEDGEMENTS

This work was supported by National Key Research and Development Program of China (Grant No. 2023YFB4502500) and National Natural Science Foundation of China (Grant No. 12034018).

## VI. DATA AVAILABILITY

The data that support the findings of this study are available upon reasonable request from the authors.

[1] R. H. Shumway, D. S. Stoffer, and D. S. Stoffer, *Time series analysis and its applications*, Vol. 3 (Springer Cham, 2000).

[2] H. Kantz and T. Schreiber, *Nonlinear time series analysis*, Vol. 7 (Cambridge university press, 2004).



- [3] M. Winterhalder, B. Schelter, and J. Timmer, *Handbook of Time Series Analysis: Recent Theoretical Developments and Applications* (John Wiley & Sons, 2006).
- [4] S. Makridakis, S. C. Wheelwright, and V. E. McGee, Forecasting: Methods and applications (second edition), *Journal of Forecasting* **3**, 457–460 (1984).
- [5] R. Fildes and K. Ord, Forecasting competitions: Their role in improving forecasting practice and research, *A Companion to Economic Forecasting*, 322–353 (2004).
- [6] P. Bauer, A. Thorpe, and G. Brunet, The quiet revolution of numerical weather prediction, *Nature* **525**, 47–55 (2015).
- [7] V. W. Y. Lam, E. H. Allison, J. D. Bell, J. Blythe, W. W. L. Cheung, T. L. Frölicher, M. A. Gasalla, and U. R. Sumaila, Climate change, tropical fisheries and prospects for sustainable development, *Nature Reviews Earth & Environment* **1**, 440–454 (2020).
- [8] S. Hochreiter and J. Schmidhuber, Long short-term memory, *Neural Computation* **9**, 1735 (1997).
- [9] K. Cho, B. van Merriënboer, C. Gulcehre, D. Bahdanau, F. Bougares, H. Schwenk, and Y. Bengio, *Learning phrase representations using rnn encoder-decoder for statistical machine translation* (2014).
- [10] H. Jaeger, *Short term memory in echo state networks* (GMD Forschungszentrum Informationstechnik, 2001).
- [11] H. Jaeger and H. Haas, Harnessing nonlinearity: Predicting chaotic systems and saving energy in wireless communication, *Science* **304**, 78 (2004).
- [12] K. Nakajima and I. Fischer, *Reservoir Computing: Theory, Physical Implementations, and Applications*, edited by K. Nakajima and I. Fischer (Springer, Singapore, 2021) pp. 423–450.
- [13] P. Rebentrost, M. Mohseni, and S. Lloyd, Quantum support vector machine for big data classification, *Phys. Rev. Lett.* **113**, 130503 (2014).
- [14] S. Lloyd and C. Weedbrook, Quantum generative adversarial learning, *Phys. Rev. Lett.* **121**, 040502 (2018).
- [15] V. Havlíček, A. D. Córcoles, K. Temme, A. W. Harrow, A. Kandala, J. M. Chow, and J. M. Gambetta, Supervised learning with quantum-enhanced feature spaces, *Nature* **567**, 209 (2019).
- [16] H.-Y. Huang, M. Broughton, M. Mohseni, R. Babbush, S. Boixo, H. Neven, and J. R. McClean, Power of data in quantum machine learning, *Nature Communications* **12**, 2631 (2021).
- [17] K. Mitarai, M. Negoro, M. Kitagawa, and K. Fujii, Quantum circuit learning, *Phys. Rev. A* **98**, 032309 (2018).
- [18] M. Schuld, R. Sweke, and J. J. Meyer, Effect of data encoding on the expressive power of variational quantum-machine-learning models, *Phys. Rev. A* **103**, 032430 (2021).
- [19] T. Goto, Q. H. Tran, and K. Nakajima, Universal approximation property of quantum machine learning models in quantum-enhanced feature spaces, *Phys. Rev. Lett.* **127**, 090506 (2021).
- [20] Z. Yu, H. Yao, M. Li, and X. Wang, Power and limitations of single-qubit native quantum neural networks (2022), [arXiv:2205.07848 \[quant-ph\]](https://arxiv.org/abs/2205.07848).
- [21] K. Fujii and K. Nakajima, Harnessing disordered-ensemble quantum dynamics for machine learning, *Phys. Rev. Appl.* **8**, 024030 (2017).
- [22] K. Nakajima, K. Fujii, M. Negoro, K. Mitarai, and M. Kitagawa, Boosting computational power through spatial multiplexing in quantum reservoir computing, *Phys. Rev. Appl.* **11**, 034021 (2019).
- [23] J. Chen, H. I. Nurdin, and N. Yamamoto, Temporal information processing on noisy quantum computers, *Phys. Rev. Appl.* **14**, 024065 (2020).
- [24] K. Fujii and K. Nakajima, Quantum reservoir computing: A reservoir approach toward quantum machine learning on near-term quantum devices, in *Reservoir Computing: Theory, Physical Implementations, and Applications*, edited by K. Nakajima and I. Fischer (Springer Singapore, Singapore, 2021) pp. 423–450.
- [25] R. Martínez-Peña, G. L. Giorgi, J. Nokkala, M. C. Soriano, and R. Zambrini, Dynamical phase transitions in quantum reservoir computing, *Phys. Rev. Lett.* **127**, 100502 (2021).
- [26] P. Mujal, R. Martínez-Peña, J. Nokkala, J. García-Beni, G. L. Giorgi, M. C. Soriano, and R. Zambrini, Opportunities in quantum reservoir computing and extreme learning machines, *Advanced Quantum Technologies* **4**, 2100027 (2021).
- [27] Q. H. Tran and K. Nakajima, Learning temporal quantum tomography, *Phys. Rev. Lett.* **127**, 260401 (2021).
- [28] L. C. G. Govia, G. J. Ribeill, G. E. Rowlands, and T. A. Ohki, Nonlinear input transformations are ubiquitous in quantum reservoir computing, *Neuromorphic Computing and Engineering* **2**, 014008 (2022).
- [29] W. D. Kalfus, G. J. Ribeill, G. E. Rowlands, H. K. Krovi, T. A. Ohki, and L. C. G. Govia, Hilbert space as a computational resource in reservoir computing, *Phys. Rev. Res.* **4**, 033007 (2022).
- [30] P. Pfeffer, F. Heyder, and J. Schumacher, Hybrid quantum-classical reservoir computing of thermal convection flow, *Phys. Rev. Res.* **4**, 033176 (2022).
- [31] Y. Suzuki, Q. Gao, K. C. Pradel, K. Yasuoka, and N. Yamamoto, Natural quantum reservoir computing for temporal information processing, *Scientific Reports* **12**, 1353 (2022).
- [32] M. Kornjača, H.-Y. Hu, C. Zhao, J. Wurtz, P. Weinberg, M. Hamdan, A. Zhdanov, S. H. Cantu, H. Zhou, R. A. Bravo, K. Bagnall, J. I. Basham, J. Campo, A. Choukri, R. DeAngelo, P. Frederick, D. Haines, J. Hammett, N. Hsu, M.-G. Hu, F. Huber, P. N. Jepsen, N. Jia, T. Karolyshyn, M. Kwon, J. Long, J. Lopatin, A. Lukin, T. Macrì, O. Marković, L. A. Martínez-Martínez, X. Meng, E. Ostroumov, D. Paquette, J. Robinson, P. S. Rodriguez, A. Singh, N. Sinha, H. Thoreen, N. Wan, D. Waxman-Lenz, T. Wong, K.-H. Wu, P. L. S. Lopes, Y. Boger, N. Gemelke, T. Kitagawa, A. Keesling, X. Gao, A. Bylinskii, S. F. Yelin, F. Liu, and S.-T. Wang, *Large-scale quantum reservoir learning with an analog quantum computer* (2024), [arXiv:2407.02553 \[quant-ph\]](https://arxiv.org/abs/2407.02553).
- [33] J. Bausch, Recurrent quantum neural networks, in *Advances in Neural Information Processing Systems*, Vol. 33, edited by H. Larochelle, M. Ranzato, R. Hadsell, M. Balcan, and H. Lin (Curran Associates, Inc., 2020) pp. 1368–1379.
- [34] Y. Takaki, K. Mitarai, M. Negoro, K. Fujii, and M. Kitagawa, Learning temporal data with a variational quantum recurrent neural network, *Phys. Rev. A* **103**, 052414 (2021).
- [35] S. Y.-C. Chen, S. Yoo, and Y.-L. L. Fang, Quantum long short-term memory, in *ICASSP 2022 - 2022 IEEE International Conference on Acoustics, Speech and Signal Processing (ICASSP)* (2022) pp. 8622–8626.
- [36] C. Xue, Z.-Y. Chen, T.-P. Sun, X.-F. Xu, S.-M. Chen, H.-Y. Liu, X.-N. Zhuang, Y.-C. Wu, and G.-P. Guo, Quantum dynamic mode decomposition algorithm for high-dimensional time series analysis, *Intelligent Computing* **2**, 0045 (2023).
- [37] M. Negoro, K. Mitarai, K. Fujii, K. Nakajima, and M. Kitagawa, Machine learning with controllable quantum dynamics of a nuclear spin ensemble in a solid (2018), [arXiv:1806.10910 \[quant-ph\]](https://arxiv.org/abs/1806.10910).
- [38] M. Negoro, K. Mitarai, K. Nakajima, and K. Fujii, Toward nmr quantum reservoir computing, in *Reservoir Computing: Theory, Physical Implementations, and Applications*, edited by



- K. Nakajima and I. Fischer (Springer Singapore, Singapore, 2021) pp. 451–458.
- [39] J. Nokkala, R. Martínez-Peña, G. L. Giorgi, V. Parigi, M. C. Soriano, and R. Zambrini, Gaussian states of continuous-variable quantum systems provide universal and versatile reservoir computing, *Communications Physics* **4**, 53 (2021).
- [40] P. Mujal, R. Martínez-Peña, G. L. Giorgi, M. C. Soriano, and R. Zambrini, Time-series quantum reservoir computing with weak and projective measurements, *npj Quantum Information* **9**, 16 (2023).
- [41] J. Dudas, B. Carles, E. Plouet, F. A. Mizrahi, J. Grollier, and D. Marković, Quantum reservoir computing implementation on coherently coupled quantum oscillators, *npj Quantum Information* **9**, 64 (2023).
- [42] J. García-Beni, G. L. Giorgi, M. C. Soriano, and R. Zambrini, Squeezing as a resource for time series processing in quantum reservoir computing, *Opt. Express* **32**, 6733 (2024).
- [43] T. Yasuda, Y. Suzuki, T. Kubota, K. Nakajima, Q. Gao, W. Zhang, S. Shimono, H. I. Nurdin, and N. Yamamoto, Quantum reservoir computing with repeated measurements on superconducting devices, arXiv preprint arXiv:2310.06706 (2023).
- [44] D. E. Rumelhart, G. E. Hinton, and R. J. Williams, Learning representations by back-propagating errors, *Nature* **323**, 533 (1986).
- [45] J. L. ELMAN, Finding structure in time, *COGNITIVE SCIENCE* **14**, 179 (1990).
- [46] M. I. Jordan, Serial order: A parallel distributed processing approach, in *Neural-Network Models of Cognition*, Advances in Psychology, Vol. 121, edited by J. W. Donahoe and V. Packard Dorsel (North-Holland, 1997) pp. 471–495.
- [47] M. Schuld, V. Bergholm, C. Gogolin, J. Izaac, and N. Killoran, Evaluating analytic gradients on quantum hardware, *Phys. Rev. A* **99**, 032331 (2019).
- [48] A. V. Uvarov and J. D. Biamonte, On barren plateaus and cost function locality in variational quantum algorithms, *Journal of Physics A: Mathematical and Theoretical* **54**, 245301 (2021).
- [49] M. Cerezo, A. Sone, T. Volkoff, L. Cincio, and P. J. Coles, Cost function dependent barren plateaus in shallow parametrized quantum circuits, *Nature communications* **12**, 1791 (2021).
- [50] C. Ortiz Marrero, M. Kieferová, and N. Wiebe, Entanglement-induced barren plateaus, *PRX Quantum* **2**, 040316 (2021).
- [51] K. Mitarai, M. Negoro, M. Kitagawa, and K. Fujii, Quantum circuit learning, *Phys. Rev. A* **98**, 032309 (2018).
- [52] A. Kandala, A. Mezzacapo, K. Temme, M. Takita, M. Brink, J. M. Chow, and J. M. Gambetta, Hardware-efficient variational quantum eigensolver for small molecules and quantum magnets, *Nature* **549**, 242 (2017).
- [53] R. LaRose and B. Coyle, Robust data encodings for quantum classifiers, *Phys. Rev. A* **102**, 032420 (2020).
- [54] K. Temme, S. Bravyi, and J. M. Gambetta, Error mitigation for short-depth quantum circuits, *Phys. Rev. Lett.* **119**, 180509 (2017).
- [55] S. Endo, S. C. Benjamin, and Y. Li, Practical quantum error mitigation for near-future applications, *Phys. Rev. X* **8**, 031027 (2018).
- [56] A. Kandala, K. Temme, A. D. Córcoles, A. Mezzacapo, J. M. Chow, and J. M. Gambetta, Error mitigation extends the computational reach of a noisy quantum processor, *Nature* **567**, 491 (2019).
- [57] A. W. R. Smith, K. E. Khosla, C. N. Self, and M. S. Kim, Qubit readout error mitigation with bit-flip averaging, *Science Advances* **7**, eabi8009 (2021).
- [58] A. Strikis, D. Qin, Y. Chen, S. C. Benjamin, and Y. Li, Learning-based quantum error mitigation, *PRX Quantum* **2**, 040330 (2021).
- [59] C. G. Broyden, The convergence of a class of double-rank minimization algorithms 1. general considerations, *IMA Journal of Applied Mathematics* **6**, 76 (1970).
- [60] R. Fletcher, A new approach to variable metric algorithms, *The Computer Journal* **13**, 317 (1970).
- [61] D. Goldfarb, A family of variable-metric methods derived by variational means, *Mathematics of computation* **24**, 23 (1970).
- [62] D. F. Shanno, Conditioning of quasi-newton methods for function minimization, *Mathematics of computation* **24**, 647 (1970).
- [63] P. Virtanen, R. Gommers, T. E. Oliphant, M. Haberland, T. Reddy, D. Cournapeau, E. Burovski, P. Peterson, W. Weckesser, J. Bright, S. J. van der Walt, M. Brett, J. Wilson, K. J. Millman, N. Mayorov, A. R. J. Nelson, E. Jones, R. Kern, E. Larson, C. J. Carey, Í. Polat, Y. Feng, E. W. Moore, J. VanderPlas, D. Laxalde, J. Perktold, R. Cimrman, I. Henriksen, E. A. Quintero, C. R. Harris, A. M. Archibald, A. H. Ribeiro, F. Pedregosa, P. van Mulbregt, and SciPy 1.0 Contributors, SciPy 1.0: Fundamental algorithms for scientific computing in python, *Nature Methods* **17**, 261 (2020).
- [64] S. Wiggins, *Introduction to Applied Nonlinear Dynamical Systems and Chaos* (Springer New York, NY, Singapore, 2003) pp. 423–450.
- [65] G. P. Tolstov, *Fourier series* (Courier Corporation, 2012).

# Supplementary Information

## Data-driven Quantum Dynamical Embedding Method for Long-term Prediction on Near-term Quantum Computers

### I. QUANTUM RESERVOIR COMPUTING

Quantum Reservoir Computing (QRC) is a useful approach for processing time series data on quantum computers. In this framework, each node is defined as a quantum orthogonal basis in Hilbert space. For a quantum state described by a density matrix in a system with  $N$  qubits, there are  $4^N$  elements. This quantum state equivalently represented as a classical state vector  $\vec{x}$  with a dimensionality of  $4^N$ , which is similar to classical reservoir computing. The state injection in QRC is described as a completely positive and trace preserving (CPTP) map on the system, represented by the transformation  $\rho_{t-1} \rightarrow \rho_s \otimes \text{Tr}_s[\rho_{t-1}]$ , where  $\rho_s$  is the subsystem used for state encoding. Then the quantum reservoir evolves under a Hamiltonian  $H$ , which is expressed as:

$$H = \sum_{i=1}^n (h + D_i) \sigma_{x,i} + \sum_{i=2}^n \sum_{j=1}^{i-1} J_{ij} \sigma_{z,i} \sigma_{z,j}, \quad (\text{S1})$$

where the disorder strength  $D_i$  and the coupling strength  $J_{ij}$  are randomly selected from uniform distributions in the interval  $[-W, W]$  and the interval  $[-J_s, J_s]$ , respectively. The transverse strength  $h$  and the disorder bound  $W$  will be expressed in units of coupling bound  $J_s$  and  $J_s = 1$  for convenience. All coefficients remain fixed during training as shown in [21, 25]. Time multiplexing is employed to enhance learning, dividing the time interval  $\tau$  into  $V$  equal subintervals to increase the number of virtual nodes. The quantum state after  $v$  subintervals' evolution is given by:

$$\rho((t-1 + v/V)\tau) = e^{-iH\tau v/V} \rho_{s_t} \otimes \text{Tr}[\rho((t-1)\tau)] e^{iH\tau v/V}, v \in \{1, 2, \dots, V\}. \quad (\text{S2})$$

Computational nodes are obtained by measuring the quantum reservoir at the end of each subinterval using a selected measurement ensemble  $O_z := \{\sigma_{z,i}, \sigma_{z,i} \otimes \sigma_{z,i+1}\}$ . The QRC output is then obtained from a linear combination of node values  $x_{ki}$ :

$$\hat{\mathbf{y}}_t = \sum_i x_{ki} w_i, \quad (\text{S3})$$

where  $x_{ki} = \text{Tr}[O_z^i \rho((k + v/V)\tau)]$  and  $i = n + vN$  represents the order in the  $v^{\text{th}}$  subinterval. The coefficients  $\{w_i\}_i$  are optimized to minimize the linear regression error between the target  $\mathbf{y}_t$  and the QRC output  $\hat{\mathbf{y}}_t$ ,

$$\min_{\mathbf{w}} \|\mathbf{y} - \mathbf{X}\mathbf{w}\|^2, \quad (\text{S4})$$

where  $\mathbf{w}$ ,  $\mathbf{y}$  and  $\mathbf{X}$  are matrix forms corresponding to  $w_i$ ,  $\mathbf{y}_t$  and  $x_{ki}$ , respectively. The main difference between QRC and our QDE method lies in the placement of training parameters. The QDE method has parameters within the circuit, whereas the QRC model's parameters are in the linear regression coefficients.

In our demonstrations, the state injection function is chosen as  $\rho(s_t) = |\Phi(s_t)\rangle \langle \Phi(s_t)|$ , where  $|\Phi(s_t)\rangle = \sqrt{(1-s_t)/2} |0\rangle + \sqrt{(1+s_t)/2} |1\rangle$ , considering the signal is one-dimensional and rescaled to the range  $[-1, 1]$ .

The learning performance is evaluated using the normalized mean square error (NMSE). The efficacy of QRC is significantly influenced by both the evolution time  $\tau$  and the number of time-multiplexing intervals  $V$ , as shown in Fig. S1. While specific values of  $\tau$ , such as  $\tau = 2.8$ , can lead to low NMSE in time series prediction, neighboring values like  $\tau = 2.6$  or  $\tau = 3.0$  may result in different performance. It is observed that the NMSE between predictions and targets decreases as the number of time-multiplexing intervals increases. However, this improvement becomes less pronounced beyond a certain point, such as when the number of intervals reaches 10, indicating a limit to the method's effectiveness compared to a lower number like 5.

Additionally, the extension of both training length and washout period, when paired with a suitable evolution time  $\tau$ , can substantially enhance the QRC's learning ability. This is clearly shown in Fig. S2, Fig. S3. In Fig. S4, we plot predicting results of the QRC model on the cosine-wave signal task, which implies that these improvements are only evident with an optimal evolution value, such as  $\tau = 0.28$ . In cases where the evolution time is not optimal, the prediction error does not decrease with increasing length. This highlights one of the significant challenges faced by QRC: the random selection of hyper-parameters in the Hamiltonian  $H$  prior to training, which significantly influences the model's learning capacity.

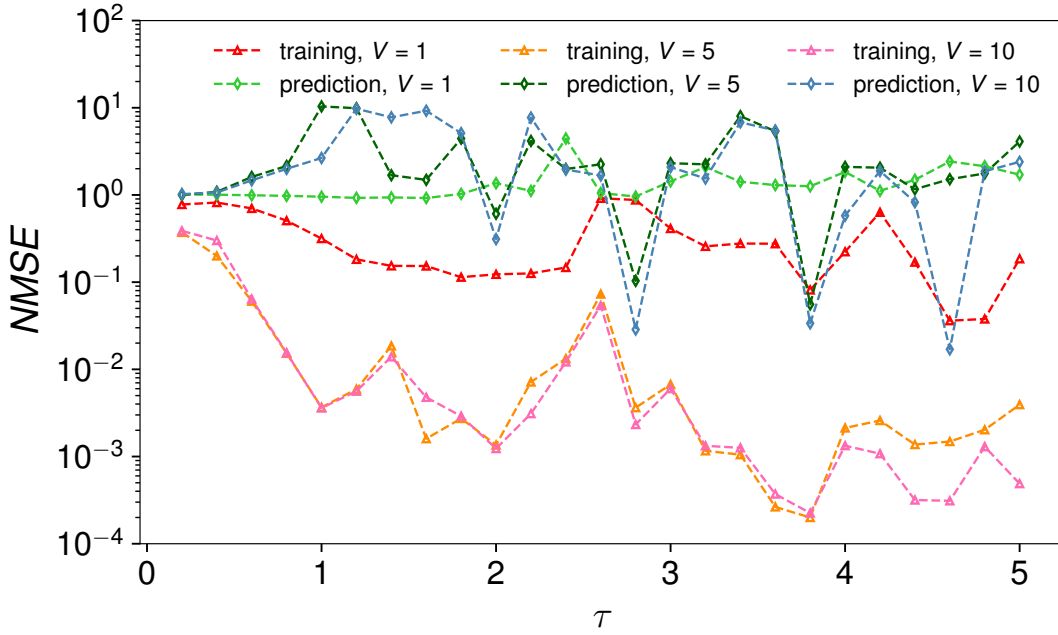


FIG. S1. Training and Predicting Error of Different Evolution Time.

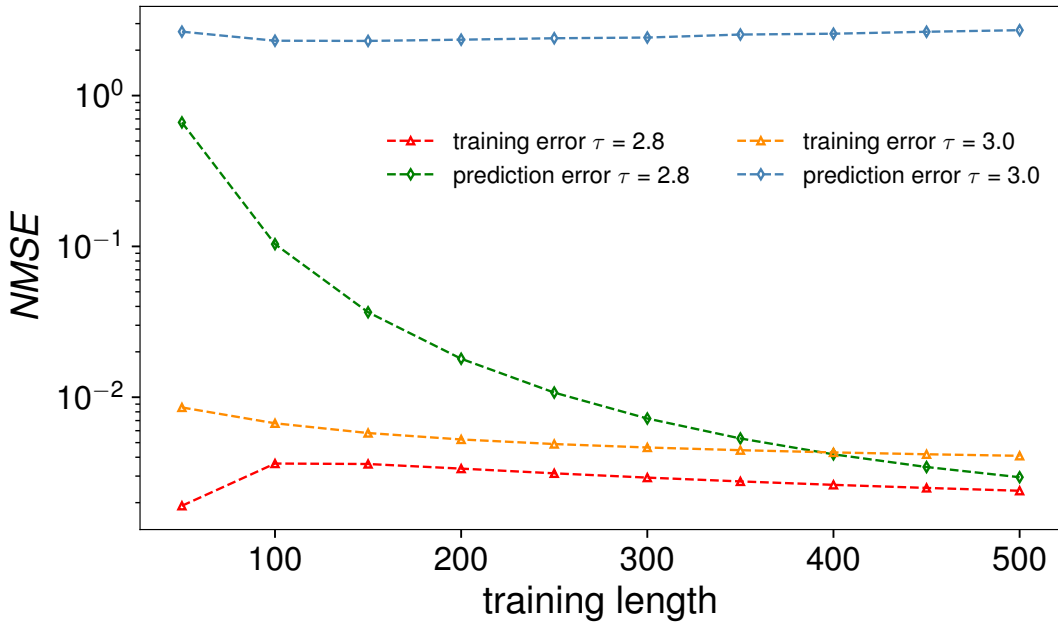


FIG. S2. Training and Predicting Error of Different Training Length.

## II. COMPARISON OF QDE WITH QRC

To compare the learning capabilities of QDE and QRC, we adjusted the hyper-parameters in Eq. (S1), sampling each Hamiltonian's coefficients uniformly within a fixed domain. MSE values are averaged over 100 realizations with the same parameter bounds for  $W$ ,  $h$ , and  $J_s$ . As shown in Fig. S5(a) and Fig. S6(a), the MSE values vary with different transverse field  $h$  and disorder bound  $W$  in units of  $J_s$ . The minimum points of the error map for the three tasks—cosine-wave signal, periodic signal, and aperiodic signal—are  $(h = 1.0000, W = 0.0479)$ ,  $(h = 1.0000, W = 0.0302)$ , and  $(h = 1.0000, W = 0.0275)$ , respectively. We also plotted the error with one parameter fixed and the other parameter varying, as shown in Fig. S5(b), (c) and Fig. S6(b),

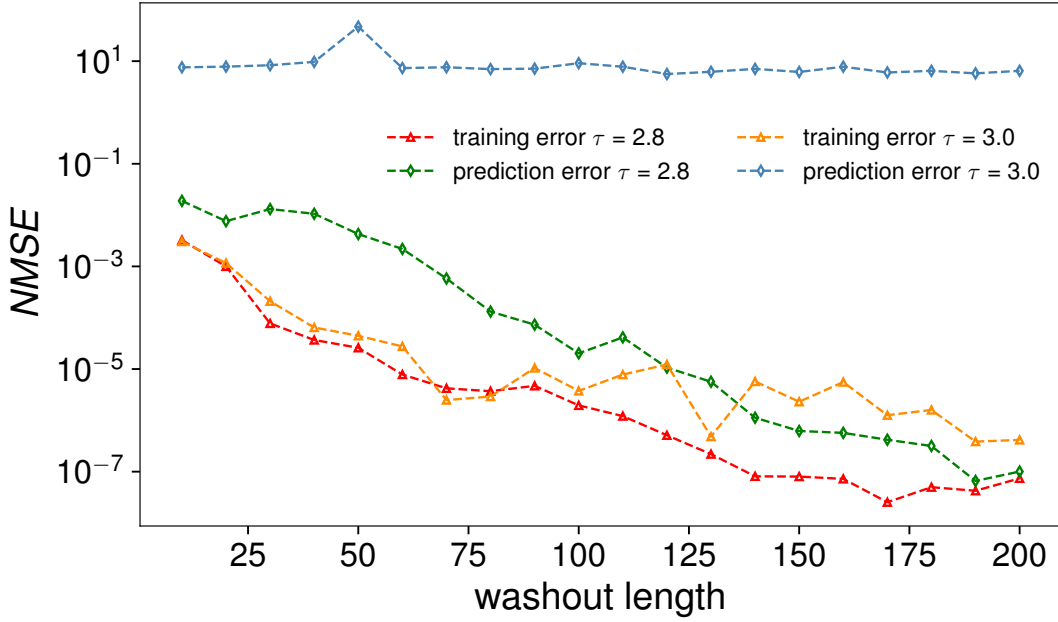


FIG. S3. Training and Predicting Error of Different Washout Time.

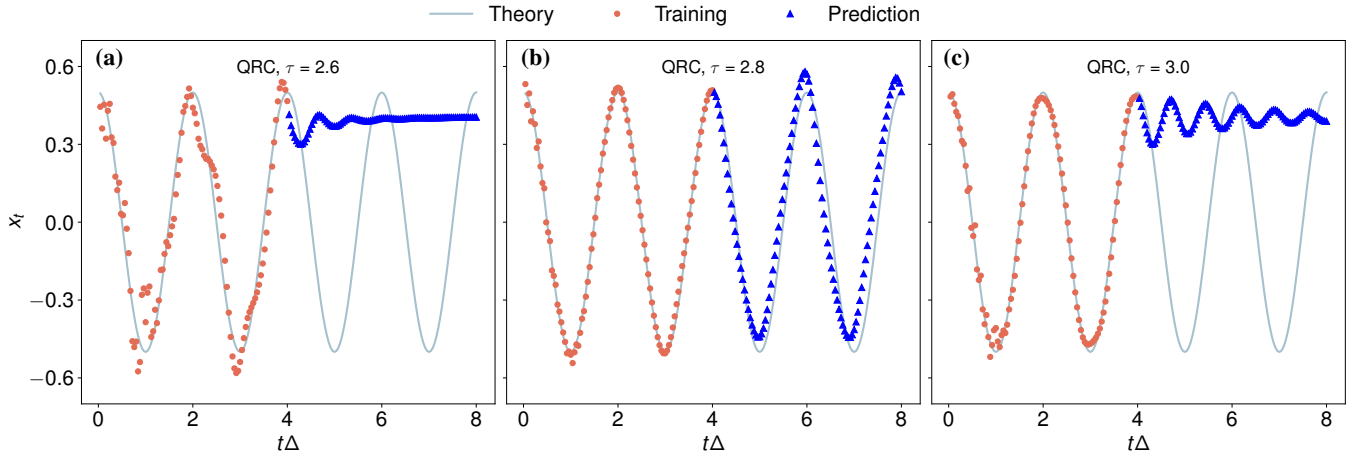


FIG. S4. **Demonstrations of QRC for Time Series Prediction:** (a), (b) and (c) are the predictions of cosine-wave from 3-qubit QRC models, varied by evolution time  $\tau$ .

(c). All these results demonstrate that our proposed method performs better than the average level of QRC.

### III. TRAINING PROCEDURES

In the training stage, the circuit parameters of the QDE are optimized using the Adam optimizer within VQNet, a quantum neural network package in Python. Here We showcase the optimization process by tracking the variation of the loss function value across training epochs.

The parameters of our architecture are divided into three components. The first comprises the rotation angles of the parameterized quantum gates. The second includes the weights and biases of the learnable error-cancellation layer as shown in main text. The final component consists of the initial values of memory from different QDE blocks.

In the simulations of a cosine-wave signal and composite signals, the QDE utilizes two linear-composite channels, each adopting the 2-qubit hardware-efficient ansatz (HEA). The simulation of the cosine-wave signal follows a similar approach but

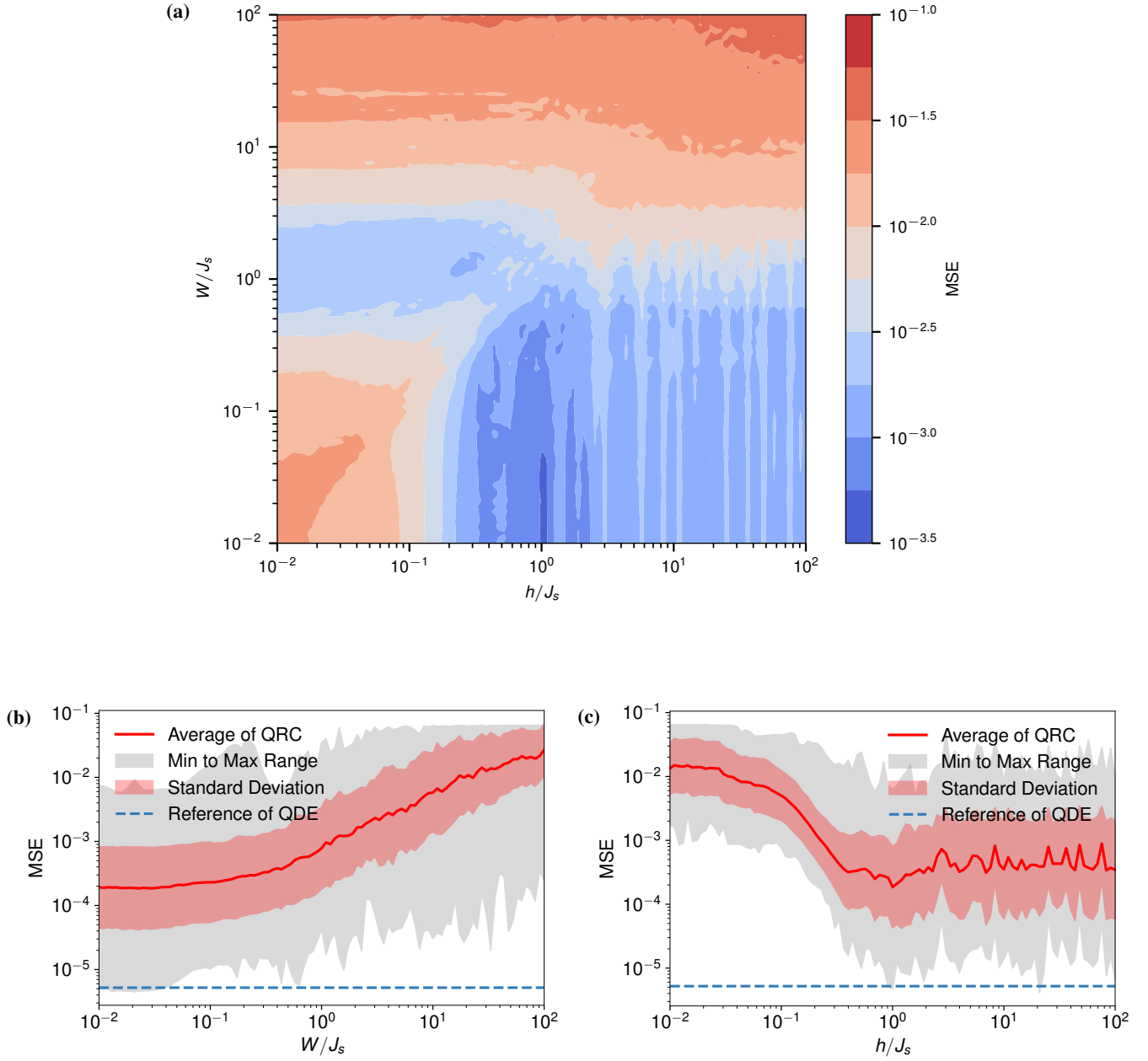


FIG. S5. **Comparison of QDE with QRC on Periodic Signal Prediction.** (a) Error map for different values of the Hamiltonian hyperparameters of QRC, with the transverse field  $h$  and the disorder bound  $W$  varying logarithmically in the range  $[10^{-2}, 10^2]$ . Results are averaged over 100 realizations. (b) and (c) With  $h/J_s$  ( $W/J_s$ ) fixed at the minimum error from map (a), the other parameter  $W/J_s$  ( $h/J_s$ ) is varied. The average results are shown with the minimum to maximum error range (grey shadows) and standard deviation (red shadows).

employs only one QDE channel. For the more complex Rayleigh dynamics, which requires modeling two-dimensional phase space and a one-dimensional hidden space, we use the transverse Ising evolution ansatz (TIEA).

During the training stage, the initial value  $(\mathbf{m}_0, \mathbf{x}_0)$  is input into the QDE model. The autoregressively generated time series  $\{\hat{\mathbf{x}}_1, \hat{\mathbf{x}}_2, \hat{\mathbf{x}}_3, \dots\}$  is then collected to compute the loss function, which is defined as mean square error. In the predicting stage, the system evolves for additional  $T$  steps to generate predictions. Here  $T$  is set to 100 and 1000 for short-term and long-term predictions, respectively.

The QRC model follows the training and predicting protocol of our approach, distinct in its data injecting method. Unlike the autoregressive feeding used in the QDE model, the QRC model is trained by feeding only the target data into the Quantum Reservoir (QR) network.



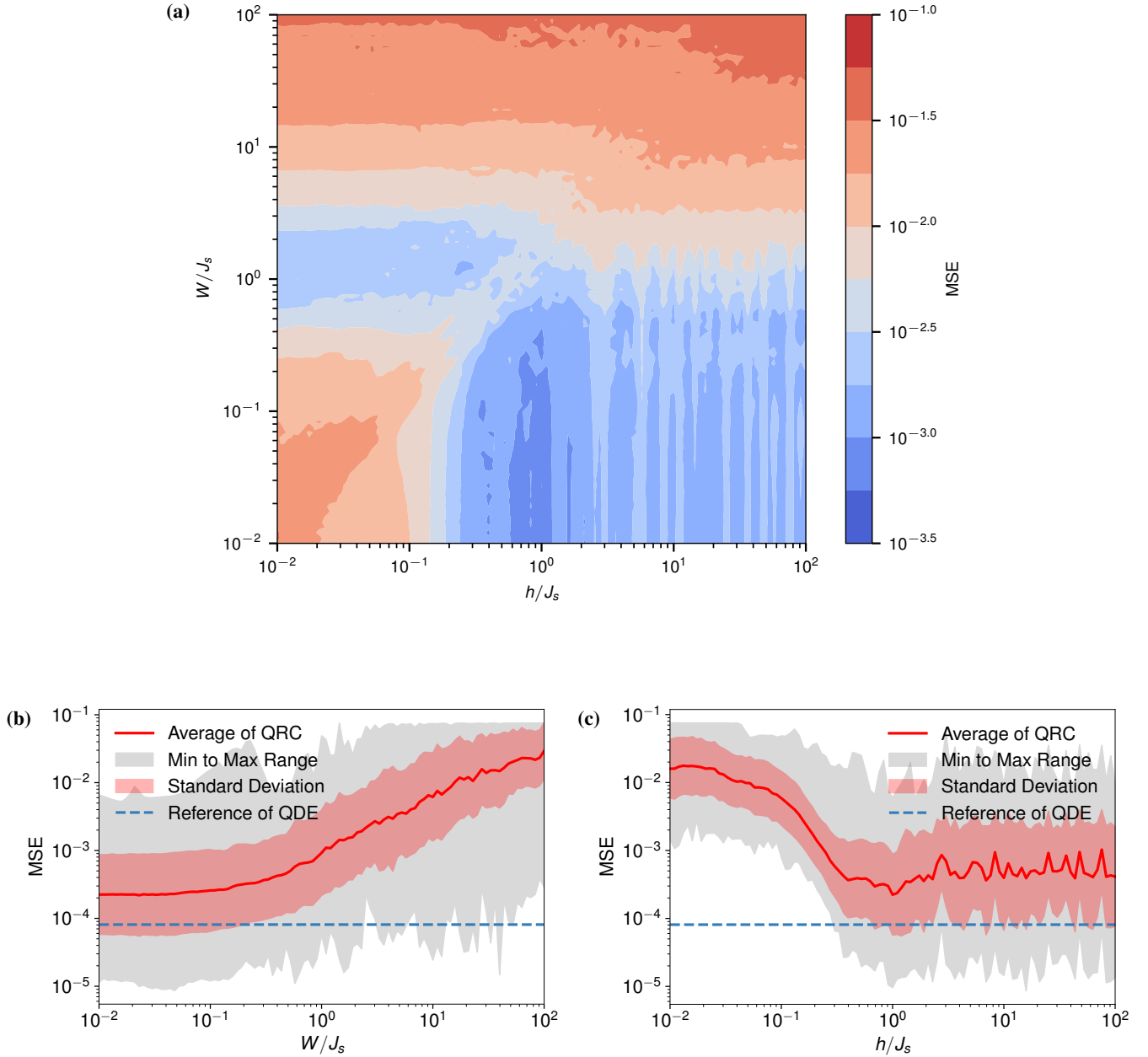


FIG. S6. **Comparison of QDE with QRC on Aperiodic Signal.** The error map and curves for different values of the Hamiltonian hyperparameters of QRC with the same settings as Fig. 3 and Fig. S5.

#### IV. QUANTUM CHIP INFORMATION

The experiment presented in the main text was executed on the Origin “Wukong” superconducting quantum computer. This platform is composed of 72 transmon qubits arranged in a two-dimensional array, with each qubit individually controlled via an XY line and Z control. The coupling strength of these qubits is adjustable from 0 to 80 MHz, and the two-qubit CZ gate operates at a strength of 50 MHz. The base frequencies of these transmon qubits are arranged in alternating high and low, the high frequency qubits have a sweetspot frequency of about 5 GHz and the low are 4.5 GHz.

Benchmarking results for single-qubit gates indicate an average fidelity for Pauli gates of 99.6%. The primary two-qubit gate of this quantum processor is the CZ gate, which achieves an average fidelity of approximately 97%. The gate time durations are 30 ns for single qubit gates and 40 ns for two-qubit gates.

Given that the experiment required only two qubits, we selected qubits Q45 and Q46 for data and memory registers of the

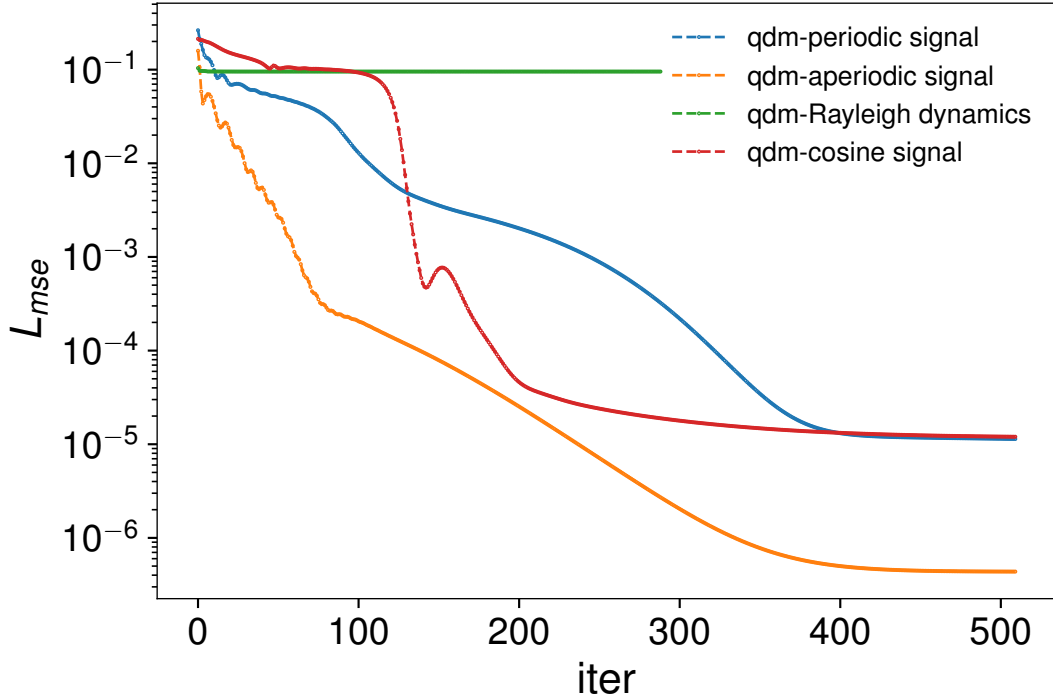


FIG. S7. Training Loss for Different Tasks

QDE. The single gate fidelities for Q45 and Q46 are 99.59% and 99.76%, respectively, with the CZ gate fidelity at 98.35%. The coherence times for these qubits are  $T_1^{45} = 11.8 \mu s$ ,  $T_2^{45} = 1.3 \mu s$  and  $T_1^{46} = 21.4 \mu s$ ,  $T_2^{46} = 0.8 \mu s$ , respectively.

Quantum circuits for the experiment were compiled using Origin Pilot and submitted through Qpandalite, a lite version of Qpanda (Quantum Programming Architecture for NISQ Device Application).

## V. ADDITIONAL EXPERIMENTS FOR LONG-TERM TIME SERIES PREDICTION

Here, we demonstrate our results for single-mode cosine-wave signal and composite periodic signal for completeness, as shown in Fig. S8 and Fig. S9. The circuit architecture, the training and predicting length, and the noisy model are the same in the main text of Sec. II and Sec. III. The consistency with the theoretical curve is kept even after 1000 steps' evolution. The decent performance of these tasks manifests the noise resistance of the proposed QDE model and the capability for capturing long-term features.

## VI. DETAILED PROOFS

Here we present detailed proofs of the Lem. 1-2 and Thm. 1-3 introduced in the main text.

*a. Proof of Lemma 1:* From a precise step  $m(t) = \hat{m}(t)$  and  $x(t) = \hat{x}(t)$ , the error produced in the next step is less than  $|\pi\Delta|/4$ .

*Proof.* For  $m$ , we have

$$\begin{aligned}
 & |m(t+1) - \hat{m}(t+1)| \\
 &= |A \sin(\pi\Delta t) [\cos(\pi\Delta) - \cos\theta] + A \cos(\pi\Delta t) [\sin(\pi\Delta) - \sqrt{1 - m_t^2 \sin^2\theta}]| \\
 &\leq A(1 - \sqrt{1 - A^2}) |\sin(\pi\Delta)| \\
 &< \frac{1}{4} |\pi\Delta|.
 \end{aligned} \tag{S5}$$

By symmetry,  $|x(t+1) - \hat{x}(t+1)|$  can also be bounded in the same way.  $\square$

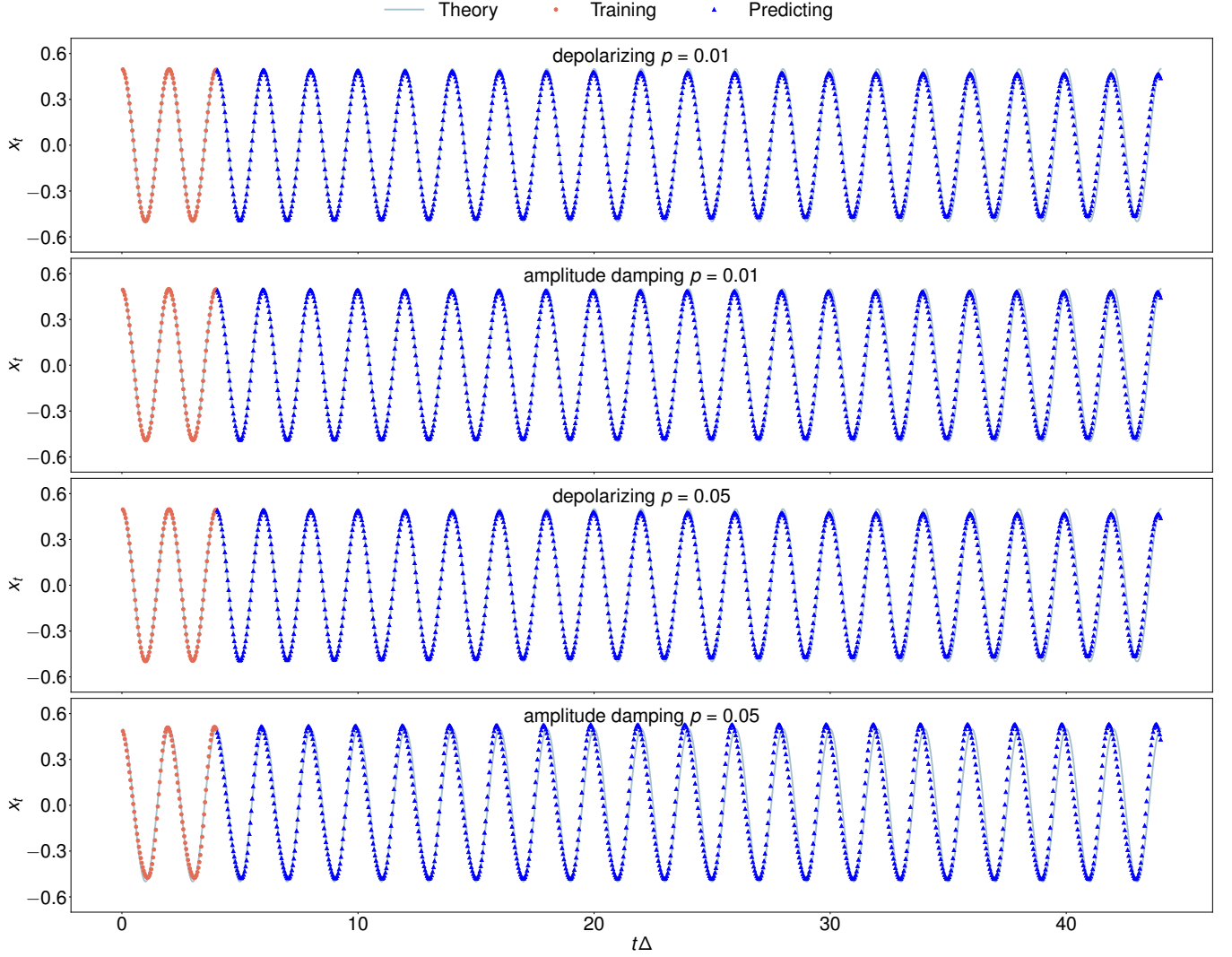


FIG. S8. **Long-term Prediction on Cosine-Wave Signal with Quantum Noise.** The training and predicting protocols replicate those in Fig. 2, with the distinction of a training-to-predicting ratio of 1 : 10.

*b. Proofs of Lemma 2:* For an erroneous step  $\hat{m}(t) = m(t) + \delta_m$  and  $\hat{x}(t) = x(t) + \delta_x$ , suppose  $|\pi\Delta| < 1/4$ , the error produce in the next step is less than  $\delta + \frac{1}{4}|\pi\Delta|$  where  $\delta = \max(|\delta_m|, |\delta_x|)$ .

*Proof.* Firstly, Consider a scenario where the error terms,  $\delta_m$  and  $\delta_x$  arise due to approximation. Assuming an error-free prior step, i.e.,  $m(t-1) = \hat{m}(t-1)$  and  $x(t-1) = \hat{x}(t-1)$ , it follows that  $\delta_m$  and  $\delta_x$  exhibit opposite signs. Without loss of generality, let  $\delta_m < 0$ , following a similar derivation as in Lem. 1.

Then, for  $m$  we have

$$\begin{aligned}
 & |m(t+1) - \hat{m}(t+1)| \\
 &= |A \sin(\pi\Delta t)[\cos(\pi\Delta) - \cos\theta] + A \cos(\pi\Delta t)[\sin(\pi\Delta) - \sqrt{1 - \hat{m}_t^2 \sin\theta}] + |\delta_m| \cos\theta - |\delta_x| \sqrt{1 - \hat{m}_t^2 \sin\theta}| \quad (\text{S6}) \\
 &\leq A(1 - \sqrt{1 - A^2})|\sin(\pi\Delta)| + \delta|\cos\theta - \sqrt{1 - \hat{m}_t^2 \sin\theta}|.
 \end{aligned}$$

Knowing that  $\pi\Delta < 1/4$ , then we derive  $|\cos\theta - \sqrt{1 - \hat{m}_t^2 \sin\theta}|_{\theta=\pi\Delta} < 1$ . Finally, we obtain

$$|m(t+1) - \hat{m}(t+1)| < \delta + \frac{1}{4}|\pi\Delta|. \quad (\text{S7})$$

By symmetry, the bound of  $|x(n+1) - \hat{x}(n+1)|$  can also established analogously.  $\square$

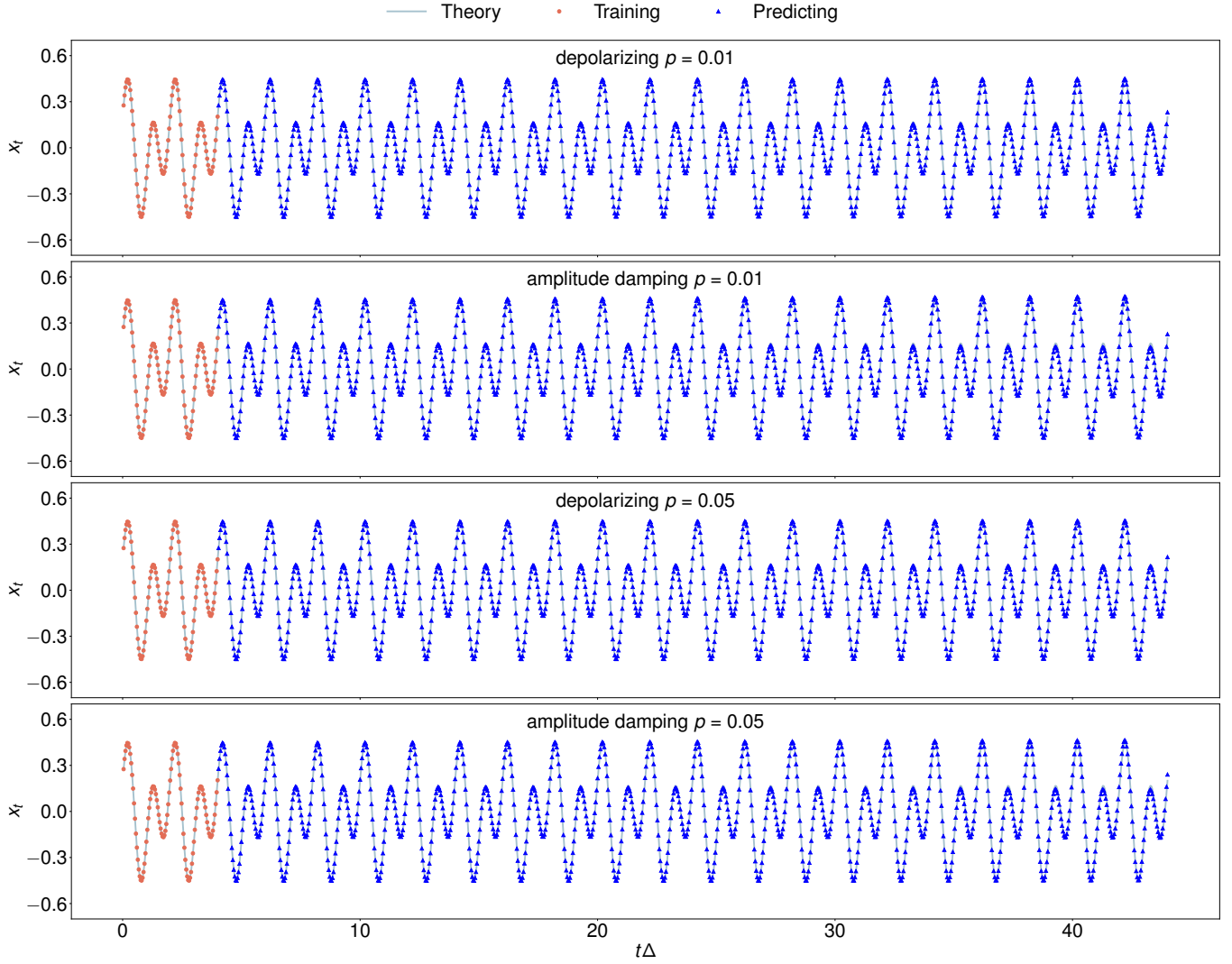


FIG. S9. Long-term Prediction on Composite Periodic Signal with Quantum Noise.

*c. Proof of Theorem 1:* By properly selecting  $\theta_1$  and  $\theta_2$ , QDE can approximate  $A \cos(\pi\Delta t + \phi)$ , where  $|A| < 1/2$ ,  $|\pi\Delta| < 1/4$  with a bounded error.

*Proof.* Firstly, the phase  $\phi$  primarily influences the initial points  $(m_0, x_0)$ , without contradicting the results of Lem. 1 and Lem. 2. For simplicity, let's set  $\phi = 0$ .

Applying Lem. 1 and Lem. 2 with the initial conditions  $m(0) = \hat{m}(0)$  and  $x(0) = \hat{x}(0)$ , and setting  $-\theta_1 = \theta_2 = \pi\Delta$ , we obtain:

$$\begin{aligned}
 |m(1) - \hat{m}(1)| &< \delta + \frac{1}{4}|\pi\Delta| \\
 |m(2) - \hat{m}(2)| &< (\delta + \frac{1}{4}|\pi\Delta|) + \frac{1}{4}|\pi\Delta| \\
 |m(3) - \hat{m}(3)| &< (\delta + \frac{2}{4}|\pi\Delta|) + \frac{1}{4}|\pi\Delta| \\
 &\vdots \\
 |m(n) - \hat{m}(n)| &< \delta + \frac{n}{4}|\pi\Delta|
 \end{aligned} \tag{S8}$$

By symmetry, the bound for  $|x(n+1) - \hat{x}(n+1)|$  can be similarly established:

$$|x(n) - \hat{x}(n)| < \delta + \frac{n}{4} |\pi \Delta| \quad (\text{S9})$$

Therefore, under the worst-case scenario, QDE approximates  $A \cos(\pi \Delta t + \phi)$  with a linearly increasing error.  $\square$

*d. Proof of Theorem 2:* Given a composite signal formed by the superposition of multiple cosine-waves,  $\sum_i^K A_i \cos(\omega_i t + \phi_i)$ , where each term has a distinct amplitude  $A_i$ , frequency  $\omega_i$  and phase  $\phi_i$ . A  $K$ -channel QDE can approximate this composite signal with a bounded error by properly selecting parameters  $\theta_1^1, \theta_2^2, \dots, \theta_1^K, \theta_2^K$ , with each superscript indexing the corresponding channel.

*Proof.* Each channel in the  $K$ -channel QDE contributes to the composite signal independently. According to Thm. 1, each individual cosine-wave component, represented by  $A_i \cos(\omega_i t + \phi_i)$ , can be approximated with a bounded error when parameters  $\theta_1^i, \theta_2^i$  are optimally selected for each channel. Finally, the composite cosine-wave can be approximated with a bounded cumulative error.  $\square$

*e. Proof of Theorem 3:* If  $g(t)$  is continuous on an interval  $[a, b]$ , then there exists a  $K$ -channel QDE approximating  $g(t)$  with a bounded error for any  $t$  in  $[a, b]$ .

*Proof.* We can choose  $c > b$  as the end of new interval  $[a, c]$ , which can be rescaled to  $[a', c']$  where  $c' - a' = 2\pi$ . Then from Cor. 2 in Sec.1 of [65], there exists a trigonometric polynomial of the form

$$\sigma_J(t') = \alpha_0 + \sum_{j=1}^J (\alpha_j \cos jt' + \beta_j \sin jt')$$

for which

$$|g(t') - \sigma_J(t')| \leq \epsilon$$

for any  $t'$  in  $[a', c']$ . The polynomial  $\sigma_J(t')$  can then be approximated using a  $K$ -channel QDE as described in Thm. 2, where in this case  $K = 2J + 1$ .  $\square$